

INVESTIGATION OF BIDIRECTIONAL REFLECTANCE AND
TRANSMITTANCE OF ROUGH SILICON WAFERS

By

YU-JIUN SHEN

A DISSERTATION PRESENTED TO THE GRADUATE SCHOOL
OF THE UNIVERSITY OF FLORIDA IN PARTIAL FULFILLMENT
OF THE REQUIREMENTS FOR THE DEGREE OF
DOCTOR OF PHILOSOPHY

UNIVERSITY OF FLORIDA

2002

ACKNOWLEDGMENTS

I would like to express my sincere appreciation to Dr. Zhuomin Zhang, chairman of my supervisory committee, for his guidance and encouragement throughout my graduate study. He provided what is certainly beyond the responsibility of a doctoral advisor. I extend my thanks to Drs. Yogi Goswami, Jacob Chung, David Hahn, and Peter Zory for graciously serving on my committee.

I also acknowledge Drs. Benjamin Tsai, Dave DeWitt, Edward Early, and Kenneth Eckerle of the National Institute of Standards and Technology for their help on the use of their instruments; and Dr. Paul Timans of the Mattson Technology, Inc. for the opportunity of collaboration. Thanks are extended to the Microscale Thermal Radiation Lab colleagues for their assistance. Among them, Qunzhi Zhu and Yihui Zhou played an important role for the experimental and theoretical part of the project.

I am indebted to Drs. Peter Sheng and C. K. Hsieh. Their recommendation brought me to this beautiful town. To my parents and dear wife, I am grateful they shared every magic moment and bitter test during my graduate study.

TABLE OF CONTENTS

	<u>page</u>
ACKNOWLEDGMENTS	ii
ABSTRACT	v
CHAPTER	
1 INTRODUCTION	1
1.1 Statement of the Problem	1
1.2 Research Objectives and Dissertation Outline	2
1.3 Significance and Justification	3
2 THEORETICAL CONSIDERATIONS	6
2.1 Rough Surface	6
2.2 Surface Scattering and BRDF/BTDF	8
2.3 Models from Physical and Geometrical Optics	11
2.3.1 Davies and Beckmann-Spizzichino Models	12
2.3.2 Torrence-Sparrow Model	14
2.4 Thick-Slab Model with Roughness Attenuation Factors	14
3 EXPERIMENTAL INSTRUMENTATION	21
3.1 STARR at NIST	23
3.2 The New Scatterometer	24
3.2.1 Goniometric Table	25
3.2.2 Light Source	26
3.2.3 Detection and Data-Acquisition System	27
3.2.4 Measurement Procedure and Uncertainty	28
3.3 <i>In situ</i> Measurement	30
3.4 Surface Profilometers	31
3.4.1 Stylus Profilometer	31
3.4.2 Optical Profilometer	32
4 PRELIMINARY RESULTS FROM STARR	49
4.1 Sample Descriptions and Surface Roughness	49
4.2 Measurements	49

4.3	BRDF Modeling Results	52
5	RESULTS FROM THE NEW SCATTEROMETER	62
5.1	Sample Characterization	62
5.2	BRDF for Wavelengths of 635 nm and 785 nm	63
5.3	Modeling Results	64
5.4	BRDF and BTDF for Wavelength of 1550 nm	67
5.5	Out-of-Plane Results	68
6	COMPARISONS OF THE NEW SCATTEROMETER WITH STARR AND <i>IN SITU</i> MEASUREMENTS	88
6.1	Comparison with Results from STARR	88
6.2	Comparison with Results from the <i>In Situ</i> Measurement	89
7	CONCLUSIONS AND RECOMMENDATIONS	95
	APPENDIX ANGLE TRANSFORMATION	98
	REFERENCES	104
	BIOGRAPHICAL SKETCH	109

Abstract of Dissertation Presented to the Graduate School
of the University of Florida in Partial Fulfillment of the
Requirements for the Degree of Doctor of Philosophy

INVESTIGATION OF BIDIRECTIONAL REFLECTANCE AND
TRANSMITTANCE OF ROUGH SILICON WAFERS

By

Yu-Jiun Shen

December 2002

Chairman: Dr. Zhuomin Zhang

Major Department: Mechanical Engineering

This research seeks to perform accurate measurements of bidirectional reflectance and transmittance of rough silicon wafers by a new benchtop scatterometer. An empirical model was developed according to the measurement data. The results will contribute to the application of radiative heat transfer modeling for a rapid thermal processing (RTP) system. In an RTP system, the radiation environment can greatly affect the reading of a lightpipe radiation thermometer. Knowledge of the bidirectional reflectance of rough silicon wafers is needed for the prediction of the reflected radiation into the radiometer, so that it can be used for accurate temperature measurement. The new scatterometer is capable of measuring out-of-plane scattering distribution at wavelengths of 635, 785, and 1550 nm from a diode laser system. Results were analyzed and compared to standard measurements at the National Institute of Standards and Technology. The relative difference is within the level of 5% for wavelengths of 635 and 785 nm and 10% for 1550 nm. An empirical model in the simple form of a two-parameter exponential function

was proposed to fit the measured data. The results show that this approach can represent the measured data better than some other theoretical models discussed in this thesis. The empirical model can be used to estimate conical reflectance around a specular direction for different collecting half-cone angles. That provides a quick way to compare specular peak measurements from different instruments with varied collecting resolution. An *in situ* measurement in the mock-up RTP chamber was also performed. Results demonstrated the feasibility of compact optics setup, which mainly uses fiber-coupled devices.

CHAPTER 1 INTRODUCTION

1.1 Statement of the Problem

The bidirectional reflectance distribution function (BRDF) and the bidirectional transmittance distribution function (BTDF) are important radiative properties in many practical applications related to the interaction of radiation with a surface or a layer. Some literature uses a more generic name, the bidirectional scattering distribution function (BSDF), which is defined as the ratio of scattered radiance to incident irradiance. The BSDF of a rough interface has been an attractive subject with considerable research devoted to theory, numerical modeling, and measurements. Usually this property is not incorporated in radiative heat transfer calculations because of the difficulty in thorough measurement and the requirement of great computational time. However, some Monte Carlo simulations show the necessity to incorporate BRDF into modeling (Hering and Smith, 1970; Zaworski et al., 1996b). Because of limitations in BSDF modeling of a complex rough surface, an accurate and thorough measurement of the surface of interest is needed.

A recent application is related to the thermometry problem in a rapid thermal processing (RTP) system (Rosa et al., 1999; Timans et al., 2000). The trend toward miniaturization of patterning features in integrated circuits has made traditional batch furnaces inadequate for many processes, including annealing and oxidization. RTP of silicon wafers has become more popular in recent years for integrated circuits

manufacturing. The major barrier for implementation of RTP in many industrial processes is accurate radiometric temperature measurement, which requires knowledge of the effective emissivity. Light-pipe radiation thermometry is the method of choice for real-time temperature monitoring in RTP (DeWitt et al., 1997; Zhang, 2000). However, the radiation environment of the RTP chamber (Fig. 1-1) can greatly affect the signal reaching the radiometer. In addition, commercial silicon wafers are usually polished only on the processed side, while the preferable arrangement is for the radiometer to view the back side (rough side) of the wafer. Knowledge of the BRDF of rough silicon wafers is needed to predict the radiation reflected into the radiometer, so that the lightpipe radiation thermometer can be used for accurate temperature measurement (Shen et al., 2001; Zhou et al., 2001).

1.2 Research Objectives and Dissertation Outline

This research aims at accurate measurements of BRDF and BTDF of rough silicon wafers by a laboratory benchtop scatterometer and an *in situ* setup in an RTP mock-up chamber. A new scatterometer (Shen and Zhang, 2002) and pseudo *in situ* measurement (Shen et al., 2002) were designed and tested. The details of the setup are described in Chapter 3, followed by a brief review of the fundamentals of surface characterization and scattering. Results were analyzed and compared using models based on the physical and geometrical optics. Based on these simplified models, an empirical approach was used to fit the measured data. This approach provides simple reflectance models for rough silicon wafers, which can approximately represent the BRDF data and be easily incorporated into Monte Carlo codes. The preliminary results from a standard facility are discussed in Chapter 4. Measurement results from the new scatterometer are

shown in Chapter 5. Based on measurement data, an empirical model with two-parameter exponential functions was fitted to the BRDF data and applied to the investigation about conical reflectance. In Chapter 6, Results from the standard instrument and comparisons are presented. Some *in situ* results are also compared with *ex situ* measurements from the new scatterometer.

1.3 Significance and Justification

This study should provide a progressively deeper understanding and a valuable BRDF/BTDF database of rough silicon wafers. The scatterometer design demonstrates an efficient way to construct the goniometric table with out-of-plane measurement ability. The BRDF/BTDF data and related models can be directly used in the existing Monte Carlo algorithm (Zhou and Zhang, 2002). Apart from the radiative heat transfer field, existing and potential applications of BSDF can be found across many disciplines including optics, optical engineering, material science, remote sensing, and computer graphics. Some examples are in the following. The effect of macroscopic roughness on the BRDF has been applied to planet observation (Hapke, 1993). In the field of computer graphics, which deals with light reflection between objects, the current trends are to include the BSDF of real surfaces and to use physically-based surface reflection models (Greenberg et al., 1997). An example of the progress is that NVIDIA Corporation (Santa Clara, CA) and Surface Optics Corporation (San Diego, CA) collaborate to implement BRDF on graphics processors for next-generation computer simulations that the military, CAD, e-business, and commercial gaming industries are seeking. Noncontact characterization of surfaces by scatterometry relies on BRDF measurements and relations between BRDF data and surface roughness parameters (Bjuggren et al., 1997; Church

and Takacs, 1995; Stover et al., 1994). Recently, two commercially available BSDF databases have been built by Stellar Optics Research International Corporation (Thornhill, Ontario, Canada) and Surface Optics Corporation. The materials cover soil, rock, vegetation, hydrology and building construction materials, fabrics, paints, and optical instrumentation materials. These data are essential to stray light analyses and are embodied into some stray light analysis programs (McCall, 2001).

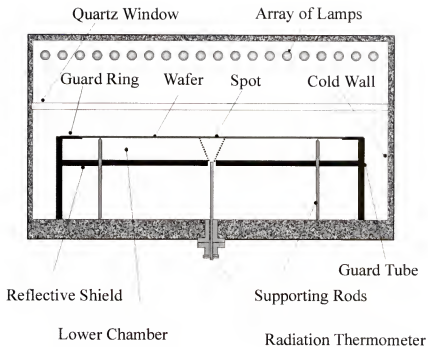


Figure 1-1 Schematic of an RTP chamber (Zhou et al., 2001).

CHAPTER 2 THEORETICAL CONSIDERATIONS

2.1 Rough Surface

Real surfaces, irrespective of their method of formation, contain irregularities or deviations from the prescribed geometrical form (Thomas, 1999). A very general classification of a rough surface is in Fig. 2-1 (Bhushan, 2001). The typology of surface height distribution depends on the nature of the processing method. Surfaces that are processed by cumulative processes, such as peening and lapping, are usually governed by the Gaussian distribution and in an isotropic form.

Some basic parameters are defined as follows. In a practical application, these parameters are obtained from the measured profile data and treated as statistical parameters for the purposes of characterization and comparison. A 1-D surface profile is considered and can be described by the height function $z(x)$. The mean height of $z(x)$ over the scanned distance L is

$$\bar{z} = \lim_{L \rightarrow \infty} \frac{1}{L} \int_L z(x) dx \quad (2.1)$$

The root-mean-square (RMS) roughness is defined in terms of surface height deviations from the mean height as

$$\sigma = \left(\lim_{L \rightarrow \infty} \frac{1}{L} \int_L [z(x) - \bar{z}]^2 dx \right)^{1/2} \quad (2.2)$$

Similarly, the RMS slope can be defined as

$$m_{rms} = \left(\lim_{L \rightarrow \infty} \frac{1}{L} \int_L \left[\frac{dz}{dx} - \bar{m} \right]^2 dx \right)^{1/2} \quad (2.3)$$

where

$$\bar{m} = \lim_{L \rightarrow \infty} \frac{1}{L} \int_L \frac{dz}{dx} dx \quad (2.4)$$

The autocorrelation function is defined by

$$C(\tau) = \frac{1}{\sigma^2} \lim_{L \rightarrow \infty} \frac{1}{L} \int_L z(x) z(x + \tau) dx \quad (2.5)$$

where τ is the translation length from the self-copied profile to the original profile. Then the autocorrelation length a is defined as the value of the translation length at which $C(\tau)$ drops to e^{-1} of its value at $\tau = 0$. Autocorrelation functions are useful for visualizing the relative degrees of periodicity and randomness of a surface profile. The autocorrelation function of a periodic surface also shows high periodicity. A random profile exhibits a strongly decaying autocorrelation function. For a Gaussian random surface, the relationship between the RMS slope and the autocorrelation length (Bennett and Porteus, 1961) is

$$a = \frac{\sqrt{2}\sigma}{m_{rms}} \quad (2.6)$$

The power spectral density (PSD) function decomposes the surface profile into its spatial Fourier component frequencies. It is defined by

$$S(f) = \lim_{L \rightarrow \infty} \frac{1}{L} \left| \int_L z(x) e^{-j2\pi f x} dx \right|^2 \quad (2.7)$$

This function plays an important role in surface characterizations since besides the raw height data of a profile, the PSD contains most of the embedded profile information.

Some parameters and functions can be calculated from the PSD. To take another Fourier transform, the autocorrelation function can be calculated as

$$C(\tau) = \frac{1}{\sigma^2} \int_{-\infty}^{\infty} S(f) e^{j2\pi f \tau} df \quad (2.8)$$

The RMS roughness and RMS slope can also be obtained as

$$\sigma = \sqrt{\int_{-\infty}^{\infty} S(f) df} \quad (2.9)$$

$$m_{rms} = \sqrt{\int_{-\infty}^{\infty} (2\pi f)^2 S(f) df} \quad (2.10)$$

The targeted surface in this study, rough side of a silicon wafer, is formed by a lapping process. The lapping process, which is before the final polishing step, removes the wafer surface damage left over from a preceded slicing process to give a nominally flat surface. The final polishing step is a combination of chemical etching and mechanical polishing. This process forms a mirror-like surface for any further patterning processes during the followed steps. The final polishing is usually done on one side of a wafer. The other side is left rough or etched. For some device use, the rough side may receive a special process to induce crystal damage, called backside damage (Zant, 2000). The typical methods are sand blasting and deposition of a polysilicon layer or a silicon nitride layer. Therefore, the rough sides of any commercial wafers may have very different roughness levels and coated layers.

2.2 Surface Scattering and BRDF/BTDF

When a beam is reflected by a rough surface, the radiation is scattered into different directions (Fig. 2-2). The angular distribution of the scattered power depends on surface roughness heights, roughness spatial wavelengths, and the wavelength of the light source (Beckmann and Spizzichino, 1963). The BRDF is for describing the nature of

reflection of a surface element and is defined (Nicodemus, 1970) as

$$f_r = \frac{dL_r(\theta_i, \varphi_i; \theta_r, \varphi_r)}{dE_i} = \frac{dL_r(\theta_i, \varphi_i; \theta_r, \varphi_r)}{L_i \cos \theta_i d\omega_i} \text{ (sr}^{-1}\text{)} \quad (2.11)$$

where (θ_i, φ_i) and (θ_r, φ_r) denote the directions of incident and reflected beams, respectively, L_i is the incident radiance, and dL_r is the reflected radiance for radiation incident from an element solid angle $d\omega_i$. The denominator of Eq. (2.11) is the incident irradiance, dE_i . The geometry of the incident and reflected beams is shown in Fig. 2-3. It is to be noted here that all the radiative properties discussed are spectral properties, which depend on the wavelength λ . The detector signal is proportional to the radiant power reaching the detector. Hence, BRDF can be calculated by the following measurement equation:

$$f_r = \frac{1}{S_i} \frac{S_r}{\cos \theta_r d\omega_r} \quad (2.12)$$

where S_i and S_r are the detector signals for the incident and reflected radiation; the ratio of S_r to S_i is a measure of the bidirectional reflectance, the solid angle $\delta\omega_r$ is approximately equal to A_r/D^2 , where A_r is the aperture area of the detector, and D is the distance between the sample and the detector aperture. If a measured sample is not opaque, the BTDF can be defined similarly as

$$f_t = \frac{dL_t}{dE_i} = \frac{dL_t}{L_i \cos \theta_i d\omega_i} \text{ (sr}^{-1}\text{)} \quad (2.13)$$

and the measurement equation is

$$f_t = \frac{1}{S_i} \frac{S_t}{\cos \theta_i \delta\omega_i} \quad (2.14)$$

The directional-hemispherical reflectance is related to the BRDF as

$$\rho_{dh} = \frac{\int_{2\pi} dL_r \cos \theta_r d\omega_r}{dE_i} = \int_{2\pi} f_r \cos \theta_r d\omega_r \quad (2.15)$$

which is a function of the incident direction.

The directional-conical reflectance and transmittance are related to BRDF and BTDF as follows,

$$\rho(\theta_i; \omega_r) = \int_{\omega_r} f_r \cos \theta_r d\omega_r' \quad (2.16a)$$

and

$$\tau(\theta_i; \omega_i) = \int_{\omega_i} f_i \cos \theta_i d\omega_i' \quad (2.16b)$$

where the solid angles are determined by the detector aperture size and arrangement.

An important principle of the BRDF is reciprocity (Siegel and Howell, 1992), which states symmetry of the BRDF with regard to reflection and incidence angles. In other words, the reflectance for energy incident from (θ_i, φ_i) and reflected to (θ_r, φ_r) is equal to that for energy incident from (θ_r, φ_r) and reflected to (θ_i, φ_i) .

Considering the limiting case of a diffuse, or Lambertian, surface, the BRDF is independent to (θ_r, φ_r) and is related to the directional-hemispherical reflectance as

$$f_{r,Lambertian} = \frac{\rho_{dh}}{\pi} \quad (2.17)$$

On the other end, the BRDF for an ideal specular, or mirror-like, surface can be represented as

$$f_{r,mirror-like} = \frac{\rho_{dh}}{\cos \theta_i} \delta(\theta_r - \theta_i) \delta(\varphi_r - (\varphi_i \pm 180^\circ)) \quad (2.18)$$

with the Kronecker delta function, $\delta(0) = 1$ and $\delta(\text{not } 0) = 0$. But no practical detectors

can resolve this singular direction. For a mirror-like surface, the use of the BRDF becomes impractical.

If the BRDF is known, one can calculate how much radiation is going to a specific direction for a given incident beam. Considering an example of a diffuse silicon surface with $\rho_{dh} = 0.32$ for 15° incidence, a near-collimated laser beam of 2 mW illuminates from the incidence angle $\theta_i = 15^\circ$. The sensor is located at 500 mm from the surface at the reflection angle $\theta_r = 30^\circ$. If the sensor area is 100 mm^2 , the solid angle $\delta\omega_r$ is estimated as $100 / 500^2 = 4 \times 10^{-4} \text{ sr}$. The BRDF for this diffuse surface is $0.32 / \pi = 0.102$. Using Eq. (2.14), the reflected power collected by the sensor is calculated as $(2 \text{ mW}) \times \cos(30^\circ) \times (4 \times 10^{-4} \text{ sr}) = 0.0007 \text{ mW}$. This example shows that typically the reflection signal of a detector varies several magnitudes with respect to the incidence signal. A large dynamic range is needed in BRDF measurements.

Another character of BRDF measurements is a large number of data generated to characterize a surface. Considering an example, one measures BRDF for every 2° of the reflection polar angle from 0° to 60° and every 5° of the azimuthal angle from $(\varphi_i + 90^\circ)$ to $(\varphi_i + 180^\circ)$. The total data points will be $31 \times 19 = 589$ for only one incidence direction.

2.3 Models from Physical and Geometrical Optics

Extensive theoretical and experimental investigations have been performed to obtain rigorous electromagnetic-wave solutions and to determine the applicable regimes for each model (Tang et al., 1999). The rigorous electromagnetic-wave solutions, however, are extremely computationally intensive. Analytical approaches with some approximations can be categorized into two groups: physical optics method and

geometrical optics method. The former usually employs the Kirchhoff approximation and the Gaussian surface assumption to model surface scattering with wave characteristics, like wave diffraction. The latter treats a rough surface as one with many small facets and uses the geometrical ray-tracing approach, which can include the multiple-scattering phenomenon. On the basis of simplicity and convenience for calculation, the following approximate models are chosen and will be compared with the experimental results.

2.3.1 Davies and Beckmann-Spizzichino Models

Davies (1954) assumed a Gaussian distribution of heights of surface irregularities about the mean level and used the Kirchhoff approximation to derive expressions for the electromagnetic energy reflected from rough surfaces. The Kirchhoff approximation is an extension of the Fresnel approximation that includes scattering but assumes that the radius of the surface curvature is smaller than the wavelength and that there is no multiple scattering (Beckmann and Spizzichino, 1963). For slightly rough surfaces ($\sigma/\lambda \ll 1$), the BRDF includes a specular component and an off-specular component in this model. The specular component is expressed as

$$f_{r,s}(\theta_i, \varphi_i) = \frac{\rho_{dh,s}(\theta_i)}{\cos \theta_i \delta \omega_i} \exp[-(4\pi \frac{\sigma}{\lambda} \cos \theta_i)^2] \quad (2.19)$$

and the off-specular component is calculated by

$$\begin{aligned} f_{r,off}(\theta_i, \varphi_i; \theta_r, \varphi_r) = & \frac{\rho_{dh,s}(\theta_i)}{\cos \theta_i \cos \theta_r} \pi^3 \left(\frac{\alpha}{\lambda}\right)^2 \left(\frac{\sigma}{\lambda}\right)^2 (\cos \theta_i + \cos \theta_r)^4 \\ & \cdot \exp\left\{-\left(\frac{\pi \alpha}{\lambda}\right)^2 [\sin^2 \theta_i + \sin^2 \theta_r + 2 \sin \theta_i \sin \theta_r \cos(\varphi_i - \varphi_r)]\right\} \end{aligned} \quad (2.20)$$

where $\rho_{dh,s}$ is the directional-hemispherical reflectance for a smooth (specular) surface and is determined by the Fresnel equations. Considering the actual measurement

conditions, the specular component, given by Eq. (2.19), exists in a finite solid angle around the specular direction (Houchens and Hering, 1967).

The Davies model is also extended to moderately rough surfaces with $\sigma/\lambda > 1$ using the following expression,

$$f_r(\theta_i, \varphi_i; \theta_r, \varphi_r) = \frac{\rho_{dh,s}(\theta_i)}{\cos \theta_i \cos \theta_r} \frac{1}{16\pi} \left(\frac{a}{\sigma}\right)^2 \exp\left[-\left(\frac{a}{2\sigma}\right)^2\right] \cdot \frac{\sin^2 \theta_i + \sin^2 \theta_r + 2 \sin \theta_i \sin \theta_r \cos(\varphi_i - \varphi_r)}{(\cos \theta_i + \cos \theta_r)^2} \quad (2.21)$$

As seen in Eq. (2.21), for very rough surfaces, the wavelength dependence comes from the Fresnel reflectance only.

Beckmann-Spizzichino model is similar to Davies model but can be applied for a broader range of roughness. First, the specularity is defined as the percentage of the reflected power at the specular direction of a rough surface ($\rho_{sp,r}$) to an ideally specular surface ($\rho_{sp,s}$). Then, a simplified relation for the specular direction can be shown as (Stagg and Charalampopoulos, 1991)

$$\frac{\rho_{sp,r}}{\rho_{sp,s}} = e^{-g} \left[1 + \delta\omega_r \cdot \pi \cos \theta_i \left(\frac{a}{\lambda}\right)^2 \sum_{m=1}^{\infty} \frac{g^m}{m!m} \right] \quad (2.22)$$

where $g = (4\pi \cos \theta_i \sigma / \lambda)^2$ is the roughness factor in the above equation. When g is a small value, the surface approaches a more specular behavior. This model also includes the scattering component around the specular direction with respect to the detector solid angle. For a latter comparison, the Davies model for the specular direction can be represented as

$$\frac{\rho_{sp,r}}{\rho_{sp,s}} = e^{-g} + \delta\omega_r \cdot \pi g \cos \theta_i \left(\frac{a}{\lambda}\right)^2 \quad (2.23)$$

2.3.2 Torrance-Sparrow Model

Torrance and Sparrow (1967) assumed that the rough surface consists of small, randomly distributed, mirror-like facets. This model is based on the geometrical-optics approximation, which neglects the phase of the electromagnetic wave. The equations for calculating the BRDF are rearranged in the following form (Burnell et al., 1995):

$$f_r(\theta_i, \phi_i; \theta_r, \phi_r) = \frac{A}{\cos \theta_i} \left[\frac{g P_{d,i,s}(\theta_d) G}{\cos \theta_r} \exp(-c^2 \alpha^2) + \cos \theta_i \right] \quad (2.24)$$

where A , c , and g are constants related to the properties of facets and the solid angle of the incident beam, G is a masking and shading function and is equal to unity in the angle range considered in the present study, and the angles α and θ_d are related to θ_i , θ_r , ϕ_i , and ϕ_r through the fundamental spherical trigonometric relations. When the reflected beam lies in the plane of incidence, $\alpha = (\theta_r - \theta_i)/2$ and $\theta_d = (\theta_i + \theta_r)/2$.

Due to the uncertainty of surface roughness measurements, fitting measurement data to all these analytical relations is performed by tuning surface roughness parameters. Another advantage of this approach is that one can use these models, which approximately represent the measured BRDF, in Monte Carlo codes.

2.4 Thick-Slab Model with Roughness Attenuation Factors

Fully characterizing the reflectance and transmittance of a layer structure with rough interfaces is a difficult task because of the scattering effect of rough interfaces and the internal multiple reflection. To have a simplified model is helpful for analyzing some experimental data that have a correlation to surface roughness. When the interface is slightly rough with respect to the wavelength, reflected radiation and transmitted radiation are still concentrated mostly in the specular (or regular for the transmitted case) direction. Without considering the angular distribution of scattered radiation, the specular

reflectance and regular transmittance can be calculated from the classical approach for thin films or thick slabs with attenuation factors related to interface roughness. Filinski (1972) used the factors from the theory by Beckmann and Spizzichino (1963). The ratio of reflectance at the specular direction of a rough surface ($\rho_{sp,r}$) to a smooth surface ($\rho_{sp,s}$) is derived as

$$\frac{\rho_{sp,r}}{\rho_{sp,s}} = \exp[-(\Delta\Phi_r)^2] \quad (2.25)$$

without considering the off-specular component. In the above equation, $\Delta\Phi_r$ is the phase difference between two reflected rays and can be written as

$$\Delta\Phi_r = \frac{4\pi\sigma n \cos\theta_i}{\lambda} \quad (2.26)$$

for a Gaussian rough surface. In Eq. (2.26), n is the refractive index of the medium; and λ is the wavelength in vacuum. After combining Eqs. (2.25) and (2.26), for the medium of air ($n \cong 1$) the relation becomes the Davies model without the off-specular part:

$$\frac{\rho_{sp,r}}{\rho_{sp,s}} = \exp\left[-\left(\frac{4\pi\sigma \cos\theta_i}{\lambda}\right)^2\right] \quad (2.27)$$

The theory is also extended to the transmission case where the phase difference can be written as

$$\Delta\Phi_{i,j} = \frac{2\pi\sigma(n_i - n_j) \cos\theta_i}{\lambda} \quad (2.28)$$

when the beam is from medium i to medium j . The ratio of the transmittance at the regular direction of a rough surface (τ_r) to a smooth surface (τ_s) is

$$\left(\frac{\tau_r}{\tau_s}\right)_{ij} = \exp\left[-\left(\frac{2\pi\sigma(n_i - n_j) \cos\theta_i}{\lambda}\right)^2\right] \quad (2.29)$$

It should be noticed that the attenuation factors could be different for the same rough interface when the beam is from opposite directions (i - j vs. j - i). This is important when the multiple reflection is considered in layers.

A simple model can be derived by using Eqs. (2.25) to (2.29) in the internal multiple reflection approach for a slab without the interference effect. This incoherent approach may be reasonable for the case with a coherent source since the interference effect is not so significant for a rough interface with respect to the case with smooth and parallel interfaces. The derived equations are summarized as follows:

$$R = \rho F_{R_{i2}} + \frac{\rho(1-\rho)^2 \tau^2 F_{i2} F_{i21}}{1 - \rho^2 \tau^2 F_{R_{i1}}} \quad (2.30a)$$

$$T = \frac{(1-\rho)^2 \tau F_{i2}}{1 - \rho^2 \tau^2 F_{R_{i1}}} \quad (2.30b)$$

where ρ and τ are the reflectance and transmittance for the smooth interface. The slab, which has refractive index n_2 , is in air. The attenuation factors are as follows:

$$F_{R_{i2}} = \exp \left[- \left(\frac{4\pi\sigma \cos \theta_i}{\lambda} \right)^2 \right] \quad (2.31a)$$

$$F_{R_{i1}} = \exp \left[- \operatorname{Re} \left(\left(\frac{4\pi\sigma n_2 \cos \theta_2}{\lambda} \right)^2 \right) \right] \quad (2.31b)$$

$$F_{i2} = \exp \left[- \left(\frac{2\pi\sigma(n_2 - 1) \cos \theta_i}{\lambda} \right)^2 \right] \quad (2.31c)$$

$$F_{i21} = \exp \left[- \operatorname{Re} \left(\left(\frac{2\pi\sigma(n_2 - 1) \cos \theta_2}{\lambda} \right)^2 \right) \right] \quad (2.31d)$$

where θ_2 is related by Snell's law, i.e., $N_2 \sin \theta_2 = \sin \theta_i$, and N_2 is the complex refractive

index. Although this is an approximate and straightforward model for rough interfaces, it is helpful to analyze experimental data quickly. Results shown in Chapter 5 are in agreement with the model calculations.

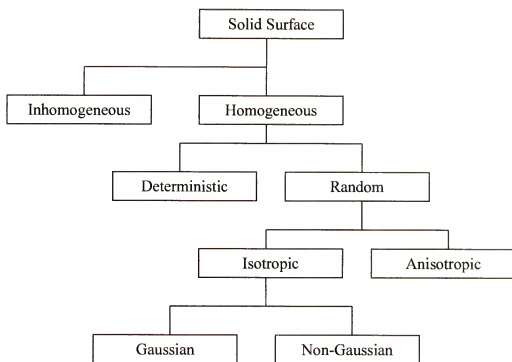


Figure 2-1 General classification of surfaces (Bhushan, 2001).

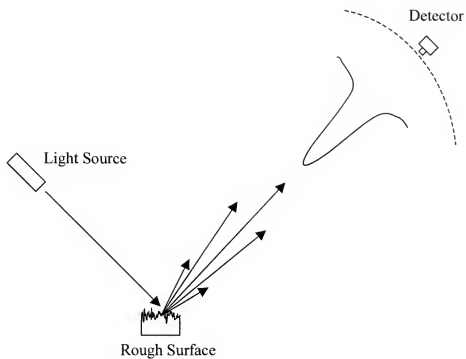


Figure 2-2 Schematic diagram of surface scattering.

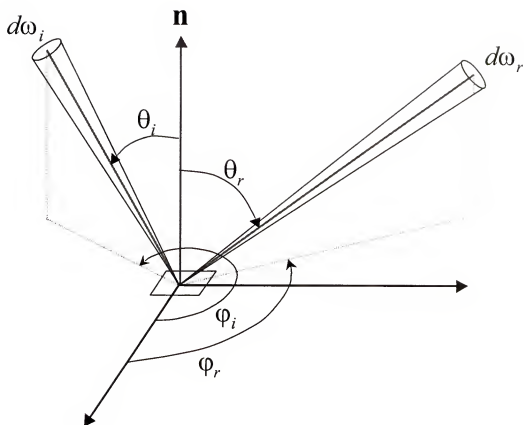


Figure 2-3 Geometry of incident and reflected beams.

CHAPTER 3

EXPERIMENTAL INSTRUMENTATION

A scatterometer, or reflectometer, is an instrument used to determine the absolute or relative scattering level of a surface. Although the sophistication of instruments may vary, most of the components may be grouped into four categories: light source, goniometric sample stage, detector, and computer system for data acquisition and control. Although the BSDF is defined in differential form, it is measured with certain limitations imposed by real instrumentation. According to Stover (1995), the following may produce some deviations between the true BSDF and the measured BSDF: the finite detector aperture, scattering created within the instrument, calibration inaccuracies, and practical equipment limitations.

The measurement wavelengths are usually within visible to near-infrared range. Difficulty in obtaining appropriate sources, detectors, and low scatter optics complicates its feasibility at wavelengths less than approximately 0.25 μm . Diffraction effects that become important for wavelengths greater than 15 μm complicate its application at longer wavelengths (McCall, 1998). The light source with necessary optics provides a near-collimated beam. Both coherent (laser) and broadband sources can be employed. Broadband sources may complicate the optical design due to employing a monochromator. Providing a continuous wavelength spectrum is its advantage. Using a coherent source (laser) is a more economical and straightforward way. However, only several limited wavelengths can be obtained from typical laser systems.

The most divergent part of the scatterometer design is the goniometric stage. It involves the movements of detector, sample, or light source. Usually, the light source is not considered to be moved due to its size and weight. A compact laser system or fiber-coupled source may be mounted on the rotary arm easily. If the light source is stationary the sample stage is expected to rotate to change incidence angles. Without considering the out-of-plane (out of incidence plane) measurements (i.e. capable of varying ϕ_r), the design is relatively easy to construct. Some examples are Zipin (1966), Drolen (1992), and Roy et al. (1993). Among this kind of design the standard is the reference reflectometer at NIST (Proctor and Barnes, 1996). If the out-of-plane measurements are needed, a more complicated hardware design is expected. Generally, there are two common designs, gimbal system (Anderson et al., 1988; Feng et al., 1993; Germer and Asmail, 1999) shown in Fig. 3-1 and circular-track system (Murray-Coleman and Smith, 1990; Zaworski et al., 1996a; White et al., 1998) shown in Fig. 3-2. Both need complicated components or much custom machining. The gimbal system needs very complicated coordinate transformation to choose the incidence and scattering angles, for example such as Germer and Asmail (1999). The polarization angle with respect to the sample may need another coordinate transformation to control. For the circular-track system, the stability and eccentricity may become a challenge for its fabrication.

Not many commercial stand-alone scatterometers are available. Among them the TASC scatterometer (Schmitt Measurement Systems, Inc., Portland, OR) and the SOC 200 series (Surface Optics Corporation, San Diego, CA) are state-of-the-art instruments that are capable of out-of-plane measurements. For the applications out of laboratories, hand-held scatterometers have been developed. The examples are the μ Scan

System (Schmitt Measurement Systems) and the SOC 600 series (Surface Optics Corporation).

3.1 STARR at NIST

The standard instrument to measure BRDF/BTDF is the spectral tri-function automated reference reflectometer (STARR) in the Optical Technology Division at NIST (Proctor and Barnes, 1996; Barnes et al., 1998). The STARR instrument is capable of measuring spectral reflectance at angles of incidence from 0° to 80° , and angles of reflection greater than 5° from the incident beam. Spectral transmittance can be measured for incidence and transmission angles up to 80° from sample normal. The main limitation is that the direction of reflection or transmission is constrained within the plane of incidence. The instrument is automatic and controlled by a computer out of the light-tight room with black walls and ceiling. Figure 3-3 shows the top view of the facility. The source subsystem contains a monochromator, two kinds of lamps, mirrors and baffles, an optical chopper, and a Glan-Taylor polarizer. A 150 W ultraviolet enhanced xenon arc lamp is used for the spectral range from 200 to 400 nm, and a 100 W quartz-tungsten-halogen lamp is for the 400 to 2500 nm spectral range. The spectral bandpass is approximately 7 nm at 550 nm. The detection subsystem consists of a cylindrical housing, a transimpedance amplifier, and a lock-in amplifier. A precision circular aperture, a fused silica lens, several baffles, and a photodiode detector are mounted in the cylindrical housing. The precision aperture defines the collection solid angle for measurements. The lens condenses the nearly collimated 14 mm diameter beam onto the detector. The collection solid angle can be approximately estimated as A_r/D^2 , where A_r is the aperture area of the detector, and D is the distance between the sample

and the aperture. For STARR, $A_r = 796.725 \text{ mm}^2$ and $D = 670.7 \text{ mm}$, indicating that the collection solid angle is 0.0017711 sr and the corresponding half-cone angle is 1.35° . Two kinds of photodiode detectors are utilized for different spectral measurements. A silicon photodiode is used for the 200 to 1100 nm range. A thermoelectrically cooled indium arsenide photodiode is used for the 900 to 2500 nm range.

Figure 3-4 shows the sample holder attached to a two axis linear positioning stage. This linear stage is mounted on a rotary stage for rotating the sample with respect to the incident beam. The detector housing is mounted on another rotary stage, which is independent of and coaxial with the sample rotary stage. The resolution and repeatability of the rotary stages are 0.001° and 0.01° , respectively. Utilizing the calibration with a white polytetrafluoroethylene (PTFE) plaque, the relative combined uncertainty ranges from 0.14 to 1.98% for the bidirectional reflectance measurements when the reflection angle lies between 0° and 80° .

The STARR is also capable of measuring the directional-hemispherical reflectance at different wavelengths and at an incidence angle of 6° , using an integrating sphere. The relative combined uncertainty for the directional-hemispherical reflectance measurements ranges from 0.21 to 0.67 % for wavelengths from 200 to 1600 nm.

3.2 The New Scatterometer

Figure 3-5 is a schematic representation of the entire apparatus, founded on a stable optical table. The scatterometer consists of three major subsystems: goniometric table, light source, and detection subsystems. The goniometric table and detection subsystem are controlled by a computer. The light source subsystem is controlled manually. The laser power and modulate frequency are set and fixed for all acquisitions.

3.2.1 Goniometric Table

As shown in Fig. 3-6 and Fig. 3-7, the goniometric table is composed of three high-accuracy rotary stages (Huber 400 series, Blake Industries, Inc., Scotch Plains, NJ) with computer-controlled step motors. Rotary stage 1, which rotates independently with respect to stage 2, varies the incidence polar angle of a vertically-stand sample holder. Considering the blocking by the sample holder frame, an 88° incidence can be achieved. Rotary stage 1 can provide a sufficient height for any insulation layers of a sample-heating compartment. An electric heater has been developed and tested on the goniometric stage, shown in Fig. 3-8 (Garcia, 2002). Another advantage of rotating the sample stage is that the stationary light source can be interchanged flexibly. The combination of rotary stages 2 and 3 provides a mean to rotate the detector over a hemisphere. The design requires only two standard rotary stages, with arm components and balance blocks, instead of some complicated parts included in a circular track or gimbal system. The rotary stages actuated by the step motors have high resolution, repeatability, and accuracy. Stage 1 has resolution of 0.005° , repeatability of 0.0006° (2"), and accuracy of 0.008° (30"). Stages 2 and 3 have resolution of 0.001° (3.6"), repeatability of 0.0006° (2"), and accuracy of 0.007° (25"). The eccentricity is below $3\text{ }\mu\text{m}$, and the wobble is within 0.0008° (3"). The operational speed can reach 5%/s. A coordinate transformation between the sample system and stage system is programmed to choose proper incidence and viewing angles. The zero angles ($\alpha = \beta = \gamma = 0$) for three rotary stages correspond to the normal incidence/reflection in the sample coordinates. The other geometric positions can be described by the following relations (see Appendix):

$$\cos \theta_r = \cos(\gamma - \alpha) \cos \beta \quad (3.1a)$$

$$\cos \varphi_r = \frac{\sin(\gamma - \alpha) \cos \beta}{\sin \theta_r} \quad (3.1b)$$

In a reflection measurement, the range of detector coverage is within $\theta_r = 0^\circ \sim 90^\circ$ and $\varphi_r = 0^\circ \sim 180^\circ$. For transparent samples, the coverage can be extended to the sample backside for measuring the BTDF. The occultation of light source by the detector tube is approximately $\pm 2^\circ$ in the incidence plane.

3.2.2 Light Source

Different light sources are employed and can be conveniently interchanged. A fiber-coupled (pigtailed) diode laser system is used to provide a coherent light source. Three diode wavelengths are employed: 635 nm (LPS-3224-635-FC), 785 nm (LPS-4224-785-FC), and 1550 nm (LPS-SMF28-1550-FC) from Thorlabs, Inc. (Newton, NJ). The maximum output power through the fiber is approximately 3 mW. The laser diode is operated in the constant-power mode through a laser current driver (Thorlabs LDC500) with a modulation function. Temperature stabilization, which is crucial to wavelength stability, is provided by a thermoelectric controller (Thorlabs TEC2000 and TCLDM9). Based on these features, the laser system has a small power fluctuation within 0.1%. Additional wavelengths can be included using different laser diodes. The light source optics setup is shown in Fig. 3-9. The fiber-coupled configuration has an advantage to maintain the system alignment when the diode laser needs to be changed since the fiber only needs to be decoupled from the collimation lens tube, which is fixed according to the alignment. The collimation lens (57CCI003, Melles Griot, Irvine, CA) gives a Gaussian beam with small divergence of 0.22 mrad ($\sim 0.0126^\circ$) and an aperture

can change the beam diameter from about 2 to 5 mm. This near-collimated beam follows the ASTM suggestion to have a unique angle of incidence (ASTM, 1997). A monochromator can be included in the future for broadband measurements. A linear polarizer (Glan-Taylor 43-6824-000, Coherent Auburn Group, Auburn, CA, and PSP series, CVI Laser Corporation, Albuquerque, NM) is used to change the polarization state of the incident light.

3.2.3 Detection and Data-Acquisition System

Silicon and germanium photodiode detectors (S2281-01, Hamamatsu Corporation, Bridgewater, NJ and J16-P2-R10M, Judson Technologies, Montgomeryville, PA) are employed to cover the wavelengths from 350 – 1100 nm and 800 – 1800 nm, respectively. Two detectors of the same type are used: one (photodiode A) on a rigid detector mount and with a precision aperture of 8 mm diameter measures the radiant power reflected or transmitted from the sample; the other one (photodiode B) monitors the incident power through a cubic beamsplitter during the whole measuring process. The advantage of this arrangement is to measure both the incident and the scattered powers without moving the sample stage. The collection solid angle can be accurately determined by the aperture area divided by the sample-to-aperture distance, 522.5 mm, indicating that $\delta\omega_r = 1.84 \times 10^{-4}$ sr and the corresponding half-cone angle is approximately 0.45° . A lock-in amplifier (Model 7265, PerkinElmer Instruments, Oak Ridge, TN) sends an oscillating signal, whose frequency is set at 1 kHz, directly to the laser current controller and measures the modulated signals from the two detectors by switching between two channels, thereby minimizing the effect of background radiation. Large dynamic range preamplifiers (Melles Griot 13AMP003) are used to maintain a near zero

bias across the photodiodes and to have a large transimpedance range from 10 to $10^9 \Omega$. A PC with the LabView (National Instruments, Austin, TX) environment performs the data acquisition and automatic rotary-stage control.

The linearity of the detection system was tested by tuning the laser diode current within its lasing range. In that range, the laser power output is basically proportional to the driving current. Different magnifications of the pre-amplifier were tested with attenuated signals by a rough wafer. The example results (Fig. 3-10) show that no significant nonlinearity exist within the power range of the instrument.

3.2.4 Measurement Procedure and Uncertainty

The procedure includes the alignment tests, beamsplitter calibration, and computer-controlled measurements. The light source (collimation lens head) is first aligned by adjusting the micrometers of the holder. The test is performed without samples on the stage and the result can be shown in a symmetric shape with respect to the viewing angles, the so-called signature plots (Fig. 3-11a). The figure only shows the results for a part of whole dynamic range using one fixed transimpedance set. Then the sample stage can be tested by some specular measurements of a mirror-like surface. The result of 10° incidence is plotted in Fig. 3-11b. The beamsplitter ratio, denoted as R_b , is defined as the signal ratio of detector A to B for the laser beams through the beamsplitter and is calibrated for both *s*- and *p*-polarizations at the condition that the detectors are underfilled by the laser beams. After the alignment tests and calibrations of R_b , the Labview routine controls the measurement process. The signal from detector B (monitoring signal), S_B is taken before and after the signal from detector A, S_A (scattering signal), and the average value is taken. The sampling period is set at 1 second and the reading number (repeat

count) is usually set from 5 to 10. By introducing the ratio R_b , BRDF is calculated by

$$f_r = \frac{S_A}{S_B \cdot R_b} \frac{1}{\cos \theta_r \delta \omega_r} \quad (3.2)$$

The measurement uncertainty can be estimated by the uncertainty propagation using Eq. (3.2), thus,

$$\frac{U_{f_r}}{f_r} = \sqrt{\left(\frac{U_{S_A}}{S_A}\right)^2 + \left(\frac{U_{S_B}}{S_B}\right)^2 + \left(\frac{U_R}{R}\right)^2 + \left(\frac{U_{\delta \omega_r}}{\delta \omega_r}\right)^2 + \left(\frac{U_{\theta_r} \sin \theta_r}{\cos \theta_r}\right)^2} \quad (3.3)$$

where U is the uncertainty due to either a bias or random uncertainty. According to the specifications and repeated measurements, the random uncertainty is about 0.2% and the bias uncertainty is about 0.65%. However, this estimation is under the assumption of perfect alignment. When misalignment exists, the last term in Eq. (3.3) will contribute greatly at large reflection angles. In addition, the signals from two detectors may be no longer perfectly correlated and may cause an additional bias uncertainty. The measured result for a mirror-like smooth surface is compared to the theoretical calculation and a relative difference of 1.5% was observed for the specular reflectance measurement.

The polished side of a commercial silicon wafer was measured as an optically smooth surface to test the instrument by comparing to the theoretical Fresnel equation. Figure 3-12 shows the measurement results at a wavelength of 635 nm for incident light with an electric field polarized in vertical (s) and horizontal (p) directions, as compared with theoretically calculated reflectance using reported optical constants of $n = 3.878$ and $\kappa = 0.0186$ at $\lambda = 635$ nm (Edwards, 1985). The agreement is quite good even at grazing angles. This demonstrates the capability of the instrument at grazing angles for a nominally uniform wafer, noticing that the illuminated area is elongated severely at such large incidence angles. A 1.5% difference was found for the unpolarized reflectance,

averaged reflectance for the two polarizations, between the measured and the theoretical calculation. This could be caused by the uncertainty in our measurements or by a difference in the optical constants of the silicon material used in the study.

3.3 *In Situ* Measurement

The feasibility of *in situ* radiative property measurement inside an RTP chamber needs further research by a compact experimental setup. These kinds of measurements can be useful for improving accuracy in pyrometric temperature measurement (Timans et al., 2000). The *in situ* measurement setup is shown in Fig. 3-13 with a picture (Fig. 3-14) of the mock-up chamber and optical accessories. The mock-up chamber was assembled after the top and bottom plates were drilled with some angled holes at angles of 0°, 30°, and 55°. The sample wafer is supported by three quartz pins whose height can be adjusted by the attached micrometers. In order to have easy alignment and a compact setup for this restricted environment, fiber-coupled solid-state light sources are employed. The light source sub-system includes a current controller and a thermoelectrically-cooled temperature regulator in order to have stable power and wavelength output. A 635 nm diode laser, 1550 nm diode laser, and 1550 nm LED can be interchanged. A fiber-coupled polarizer with a polarization maintaining (PM) fiber (OZ Optics, Carp, Ontario, Canada) provides linearly polarized light. The polarization axis is aligned with the fiber connector notch. The lens after the PM fiber gives a collimated beam, which is incident at the wafer center. Si and Ge photodiode detectors are used for the 635 nm and 1550 nm measurements, respectively. A lens mounted on the hole used to collect reflected light acts as an aperture for the detector. The signals are recovered by the lock-in amplifier which sends a specific modulation frequency to the light source current

controller. An incident power measurement was taken with the wafer removed from the chamber in the direct transmission mode. The reflectance or transmittance of the wafer is obtained as the ratio of the reflected or transmitted signals to the incident signal. The incident power measurements were repeated several times during the measurements to ensure that the laser power was stable and the alignment had not changed. The measurements were taken through manual alignment and data acquisition. The collection solid angles, ω , can be estimated by the area of the aperture, A , divided by the sample-to-aperture distance, d . For the 30° holes, they are calculated as $\omega_r = 0.00381$ sr ($d_r = 76.1$ mm, $A_r = 22.06$ mm²) for the reflection measurements and $\omega_t = 0.00304$ sr ($d_t = 85.25$ mm, $A_t = 22.06$ mm²) for the transmission measurements. The corresponding half-cone angle is approximately 2° .

3.4 Surface Profilometers

There are two classifications of surface metrology: contact and non-contact profilometry. In this study, a stylus profilometer and an optical profilometer are used at the Major Analytical Instrumentation Center, Department of Material Science and Engineering, University of Florida. The former belongs to contact metrology and the latter non-contact metrology.

3.4.1 Stylus Profilometer

The stylus profilometer, Surfometer Series 400 (Precision Devices, Inc., Milan, MI), uses a fine-diamond stylus to traverse a surface. A schematic is shown in Fig. 3-15. As the stylus travels along the surface profile, its vertical motion is converted to a time-varying electrical signal by a transducer. An A/D converter with a microprocessor will digitize, store, and process the profile information for the desired surface parameters.

The diamond tip size is approximately $5\text{ }\mu\text{m}$ and the typical stylus force is less 0.016 N . The measurement range of peak to valley is $150\text{ }\mu\text{m}$. The stroke length can be adjusted from 1.27 mm to 12.7 mm . The vertical resolution is in the nanometer range but the lateral resolution is about several micrometers. The advantage of a stylus instrument is that coating or semitransparent samples do not affect its performance. The drawback is its slow measurement speed for 2-D area scanning.

3.4.2 Optical Profilometer

Here we refer an optical profilometer as an instrument using the interferometry method to picture surface heights. A popular commercial product, Wyko NT1000 (Veeco Metrology Group, Tucson, AZ), is used in this study. This instrument contains following basic components (Fig. 3-16): a Mirau interferometer with a microscope objective, a white-light source, a beamsplitter, and a CCD camera. The interferometer provides a system where one beam is reflected from the surface under test and the other beam is reflected from a reference mirror. The beams are recombined to create fringes that represent the surface topography. Through the CCD detector, these fringes are processed by the corresponding phase-mapping programs according to the selected mode. There are two modes for different applications: the PSI (Phase Shifting Interferometry) mode and the VSI (Vertical Scanning Interferometry) mode (Olszak et al., 2001). The PSI mode is for measuring extremely smooth surfaces and features, such as mirrors, optics, and magnetic heads of hard disk drives. For a rough silicon wafer, the VSI mode is proper. The basic mechanism is that a surface is scanned vertically and then the processing program locates the exact vertical position of a resolved point where each signal reaches

its maximum amplitude (Caber, 1993). Unlike the 1-D line scanning by the stylus instrument, this optical profilometer can scan a 2-D area very fast.

This instrument under VSI mode can provide a vertical resolution in the nanometer range. However, the lateral resolution is limited by the optical components and the CCD camera pixel density. The lateral resolution is about 80 nm at the maximum magnification. A trade-off issue is of a very small sampling area under this maximum magnification. When a larger sampling area is needed, the lateral resolution may be enlarged to about 1 μm . Another potential issue is the effect of coating and semitransparent samples. The more complicated interference effect may confuse the instrument to represent a wrong height. Some measurements compared with the results by an atomic force microscope show the coating effect indeed draws an additional uncertainty (Zhu et al., 2002).

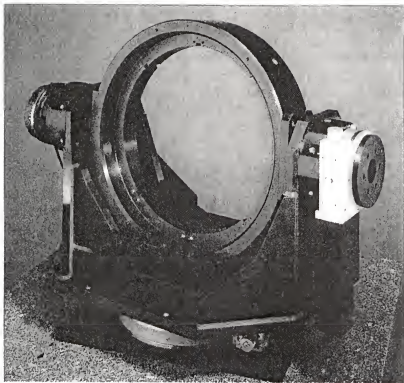


Figure 3-1 Gimbal system (Newport Corp.).



Figure 3-2 Scatterometer with a circular track (Schmitt Measurement Systems, Inc.).

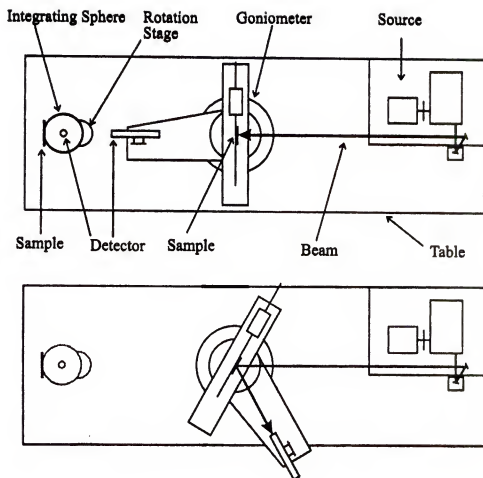


Figure 3-3 Schematic of the STARR instrument at NIST.

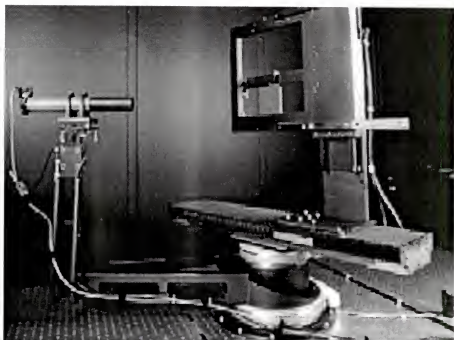


Figure 3-4 STARR instrument showing the goniometric stage.

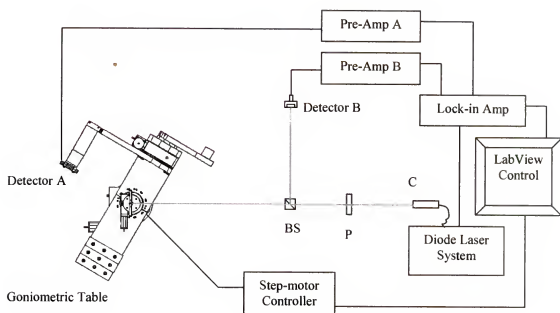


Figure 3-5 Schematic of the new scatterometer instrument (not to scale).
BS: Beamsplitter; P: Polarizer; C: Collimation lens.

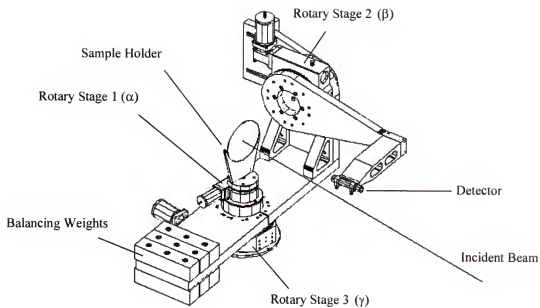


Figure 3-6 Goniometric table showing the arrangement of three rotary stages. The rotation angles about their axes are denoted by α , β , and γ , respectively.



Figure 3-7 Goniometric table.

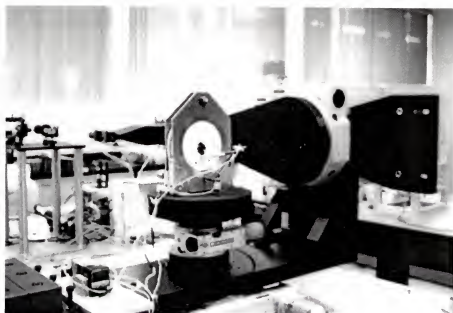


Figure 3-8 Goniometric table with the heated sample holder.

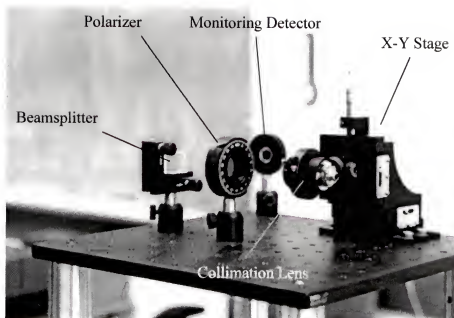


Figure 3-9 Light source optics setup.

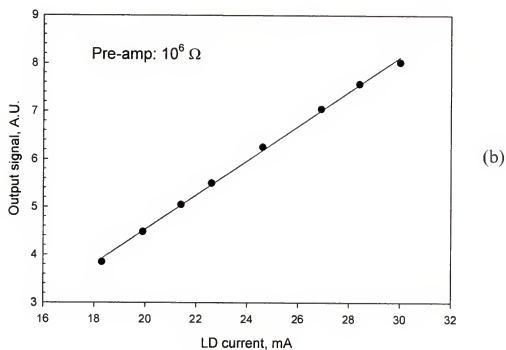
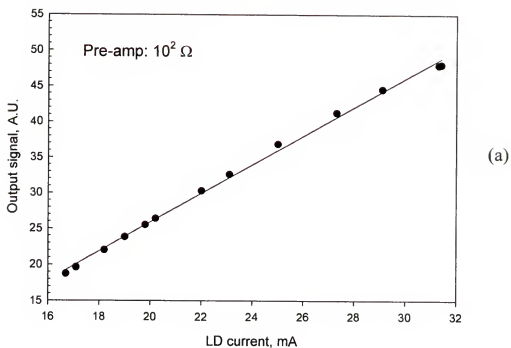
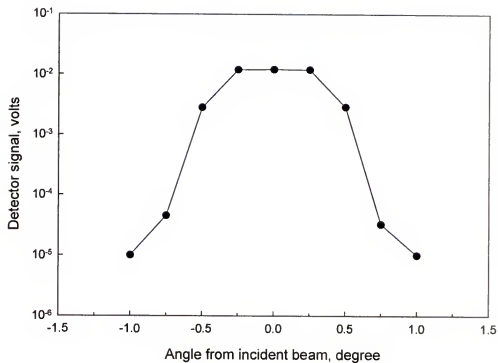
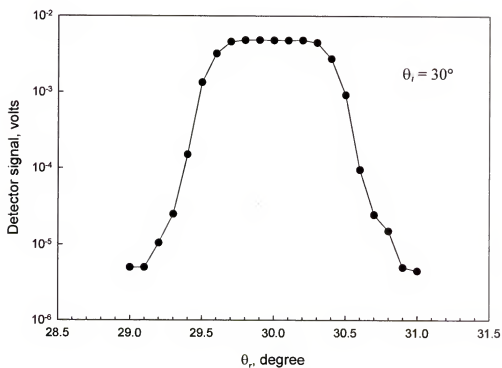


Figure 3-10 Linearity test on the detection system for the pre-amplifier range at (a) $10^2 \Omega$ and (b) $10^6 \Omega$. The output signal units are arbitrary.



(a)



(b)

Figure 3-11 (a) Alignment test without samples; (b) Alignment test with a mirror-like sample.

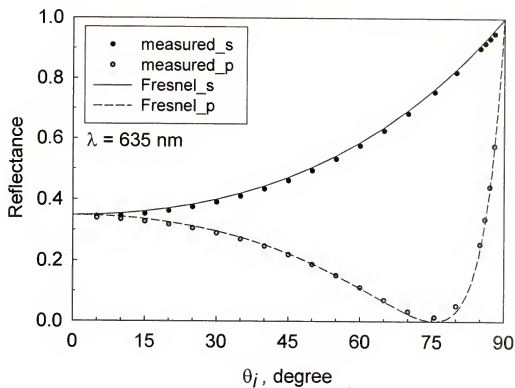


Figure 3-12 Specular reflectance of the polished side of a silicon wafer, compared to the Fresnel equation.

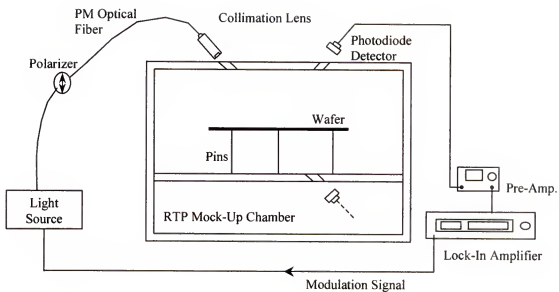


Figure 3-13 Schematic of the *in situ* measurement setup.

Detector

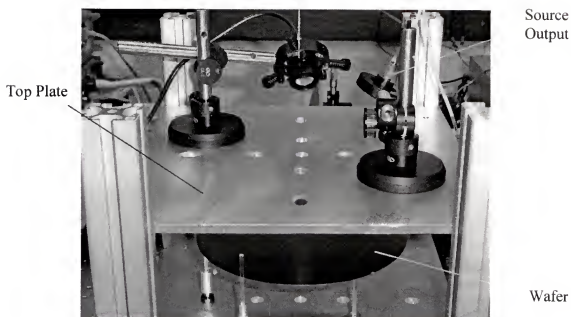


Figure 3-14 A close look at the detector and top plate

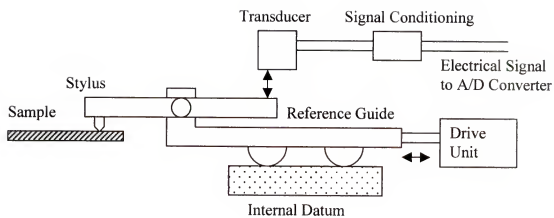


Figure 3-15 Schematic of a stylus profilometer.

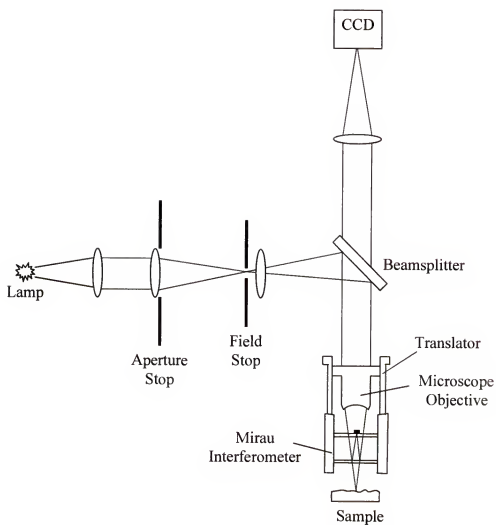


Figure 3-16 Schematic of the optical interferometric profilometer.

CHAPTER 4 PRELIMINARY RESULTS FROM STARR

4.1 Sample Descriptions and Surface Roughness

Using the optical profilometer discussed in Chapter 3, the RMS roughness averaged over three different spots ($606 \mu\text{m} \times 461 \mu\text{m}$ area) and their standard deviations are measured and listed in Table 4-1 for four surfaces, labeled as A, B, C, and S. The surface images of surfaces A, B, and C are represented in Fig. 4-1. Surfaces A and B are the rough sides of two silicon wafers of 200 mm diameter and 0.8 mm thickness. These two surfaces may have been coated with oxide or nitride layers since their appearances are purple (surface A) and blue (surface B). Surface C is the rough side of a silicon wafer of 150 mm diameter and 0.6 mm thickness. A smooth surface, labeled S, is the polished side of the same wafer of surface B.

4.2 Measurements

In the measurements, the reflected beam is constrained within the plane of incidence, i.e., ϕ_i and ϕ_r are related by either $\phi_r = \phi_i$ or $\phi_r = \phi_i \pm \pi$. Therefore, the BRDF data are presented in terms of an observation angle, defined as

$$\theta_{obs} = \begin{cases} \theta_r & \text{for } \phi_r = \phi_i \pm \pi \\ -\theta_r & \text{for } \phi_r = \phi_i \end{cases} \quad (4.1)$$

The measured BRDF of surfaces A, B, and C at the wavelength of 950 nm are shown in Fig. 4-2 for incidence angles of 10° and 45° . The data represent the average values for p-polarization (where the electric field is parallel to the plane of incidence) and

s-polarization (where the electric field is perpendicular to the plane of incidence). All curves are nearly symmetric about the specular angle, $\theta_{obs} = \theta_i$, where the BRDF is the greatest. In general, a rougher surface should show a lower specular reflection and a more uniform angular distribution due to surface scattering. Surface C, the roughest one, clearly shows a much smaller BRDF value at the specular angle (more than an order of magnitude smaller than those of surfaces A and B). The angular variation of surface C is much smaller compared with other samples. In fact, the BRDF values, away from specular, for surface C are greater than those for surfaces A and B. It is interesting to note that for surface C, there exist subsidiary maxima at observation angles about 45° from the specular. Similar scattering results were seen for rough dielectric surfaces (due to multiple scattering) (Chaikina et al., 1997), and rough thin metallic films (due to the combined effect of multiple scattering and interference) (Lu and Maradudin, 1997). If we treat the subsidiary peaks as from a grating surface, it implies that there may be a feature with the lateral characteristic length of $\sim 1.52 \mu\text{m}$. The BRDF for surface B decreases most rapidly away from the specular angle, although the value at the specular angle for surface B is slightly smaller than that for surface A. The measured rms roughness for surface B is the smallest as expected. However, the abnormal behavior of the specular values indicates that the surface coatings may have affected the BRDF and roughness measurements. This is also shown by the measured directional-hemispherical reflectance of surface A, $\rho_{dh} = 0.81$, which indicates a possible coating effect.

The directional-hemispherical reflectance and the BRDF values at the specular angle for surface C are shown in Fig. 4-3 for $400 \text{ nm} < \lambda < 1100 \text{ nm}$. Notice that the directional emissivity is equal to $1 - \rho_{dh}$. The smooth curve in Fig. 4-3a is calculated from

the Fresnel equations using the refractive index (n) and extinction coefficient (κ) of silicon (Edwards, 1985). The measured ρ_{dh} agrees well with the theoretical values for smooth surfaces (except for $\lambda = 1100$ nm). For dielectric materials, surface roughness has little impact on the emissivity, unless the specimen is semi-transparent or the roughness is large enough to cause multiple scattering (Timans, 1996). The larger ρ_{dh} measured at 1100 nm could be caused by the reflection from the other surface of the wafer since the absorption coefficient of silicon decreases rapidly as the wavelength is increased around 1100 nm (corresponding to the energy gap of silicon). In addition, the silicon diode used in these measurements almost reaches its detection limit at $\lambda = 1100$ nm, which may cause a large measurement uncertainty. In Fig. 4-3b, the calculated values are based on the Fresnel reflectance multiplied by a constant. In other words, the BRDF depends on the wavelength only through the refractive index and extinction coefficient. This is valid when the RMS roughness is much greater than the wavelength as predicted by the theoretical models discussed in Chapter 2. The constant is set to the ratio of the measured BRDF to the Fresnel reflectance at $\lambda = 950$ nm.

The BRDF data are employed to estimate the directional-hemispherical reflectance using Eq. (2.15). Since the BRDF data are limited within the plane of incidence, the assumption of an isotropic surface is made to perform the integration along the azimuthal direction. The calculated ρ_{dh} are 0.78, 0.27, and 0.53 for surfaces A, B, and C, respectively, whereas the measured values are correspondingly 0.81, 0.32, and 0.31. The large differences may be caused by the limited data used in the integration, especially near the specular direction, and the assumption of isotropic surfaces. The

existence and shape of subsidiary maxima in the out-of-incidence planes of surface C should be further investigated.

Reflectance measurements for surface S were also made. The surface can be considered optically smooth and should be described by the Fresnel reflection equations. The measured specular reflectance at 10° incidence angle is 0.317 (averaged over $\rho_{\perp} = 0.322$ for s-polarization and $\rho_{\parallel} = 0.312$ for p-polarization), which compares well with the theoretical value of 0.3195 ($\rho_{\perp} = 0.325$ and $\rho_{\parallel} = 0.314$), calculated from the Fresnel equations with an estimated refractive index $n = 3.6$ at $\lambda = 950$ nm (Edwards, 1985). However, the measured specular reflectance is 0.288 ($\rho_{\perp} = 0.397$ and $\rho_{\parallel} = 0.179$) at 45° incidence angle, which is much smaller than the theoretical value of 0.3204 ($\rho_{\perp} = 0.444$ and $\rho_{\parallel} = 0.197$). This unexpected large discrepancy needs further investigation.

4.3 BRDF Modeling Results

Comparisons between the measured data and model calculations for surfaces B and C are shown in Figs. 4-4 and 4.5, at $\lambda = 950$ nm and for $0^\circ \leq \theta_r \leq 60^\circ$. Some parameters in the models are obtained by fitting the BRDF data. The fitting process, except for the specular data point in the slightly rough Davies model, is performed by an iterative algorithm, the Marquardt-Levenberg method (Press, 1992), to obtain a convergent result. In the model for slightly rough surfaces, the off-specular component is fitted first, using Eq. (2.20), to obtain the roughness parameters α and σ . At the specular angle, the summation of the specular component, Eq. (2.19), and the off-specular component, Eq. (2.20), is fitted to the data point to obtain an additional parameter, $\delta\omega_s$,

which was not known exactly in the experiments. Because the angular dependence of $\rho_{dh,s}(\theta)$ averaged over the two polarizations is small for $\theta \leq 45^\circ$, it is assumed to be a constant, equal to 0.81 for surface A or 0.32 for surface B, to simplify the fitting process. The fitting parameters for different models are listed in Table 4-2

For surface B, the Davies model for slightly rough surfaces is used to fit the measured data at a 10° incidence angle, as shown in Fig. 4-4a. The optimal fitting parameters obtained by fitting the data for the 10° incidence angle are then used to calculate the BRDF for the 45° incidence angle, as shown in Fig. 4-4b. The model approaches approximately the variation in BRDF data, but the relative difference in the calculated and measured values at the specular angle for the 45° incidence angle is 14.6%. The fitted σ is smaller than the measured value of $0.13 \mu\text{m}$, and $\delta\omega_i$ is greater than $\delta\omega_r$. The surface coatings may have influenced the BRDF and roughness measurements; hence, the model considering pure silicon may not be suitable to predict the actual behavior. For surface A, the same model can be fit to the data approximately with different parameters using $\rho_{dh} = 0.81$, but the deviation is larger due to the possible coating effect. For surfaces A and B, good agreement could not be obtained using the Torrance-Sparrow model because the geometrical-optics approximation is applicable for relatively rough surfaces only.

For surface C, both the Davies model for rough surfaces and the Torrance-Sparrow model are fitted to the BRDF data at 10° incidence angle, as shown in Fig. 4-5a. The Torrance-Sparrow model can fit the data well for $\theta_r < 40^\circ$, whereas the fitting results of the Davies model are not as good since there is only one adjustable parameter. At large reflection angles, the BRDF calculated from the Davies model

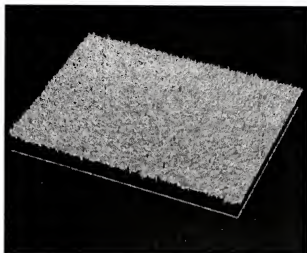
approaches zero, while that calculated from the Torrance-Sparrow model approaches a constant, equal to A in Eq. (2.24). Both models failed to predict the subsidiary peaks at about 45° from the specular angle. The same fitting parameters are used to calculate the BRDF for 45° incidence angle and compared with the data, as shown in Fig. 4-5b. Compared with the measured results, the curve calculated from the Torrance-Sparrow model is slightly shifted towards the right.

Table 4-1 Sample Surfaces of Different Silicon Wafers

Surface label	A	B	C	S
Diameter (mm)	200	200	150	200
Wafer thickness (mm)	0.8	0.8	0.6	0.8
Rms roughness σ	0.23 μm	0.13 μm	0.94 μm	1.08 nm
Standard deviation	0.003 μm	0.002 μm	0.04 μm	0.2 nm

Table 4-2 Values of Fitting Parameters

Surface	A	B	C	
Model	Davies (slightly rough)	Davies (slightly rough)	Davies (rough)	Torrance- Sparrow
Parameters	$\sigma = 0.07 \mu\text{m}$ $a = 2.2 \mu\text{m}$ $\delta\omega_t = 0.0078 \text{ sr}$	$\sigma = 0.06 \mu\text{m}$ $a = 2.7 \mu\text{m}$ $\delta\omega_t = 0.0036 \text{ sr}$	$a / \sigma = 22$	$A = 0.124$ $c = 13.5$ $g = 80$

**Surface A**

Field size: $606\ \mu\text{m} \times 461\ \mu\text{m}$

RMS roughness: $0.23\ \mu\text{m}$

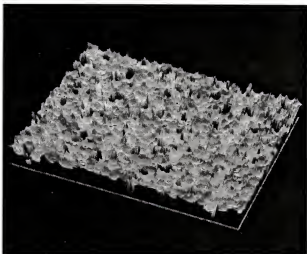
Max. peak-valley distance: $4.97\ \mu\text{m}$

**Surface B**

Field size: $606\ \mu\text{m} \times 461\ \mu\text{m}$

RMS roughness: $0.13\ \mu\text{m}$

Max. peak-valley distance: $2.14\ \mu\text{m}$

**Surface C**

Field size: $606\ \mu\text{m} \times 461\ \mu\text{m}$

RMS roughness: $0.94\ \mu\text{m}$

Max. peak-valley distance: $7.74\ \mu\text{m}$

Figure 4-1 Surface profiles for the three surfaces, A, B, and C.

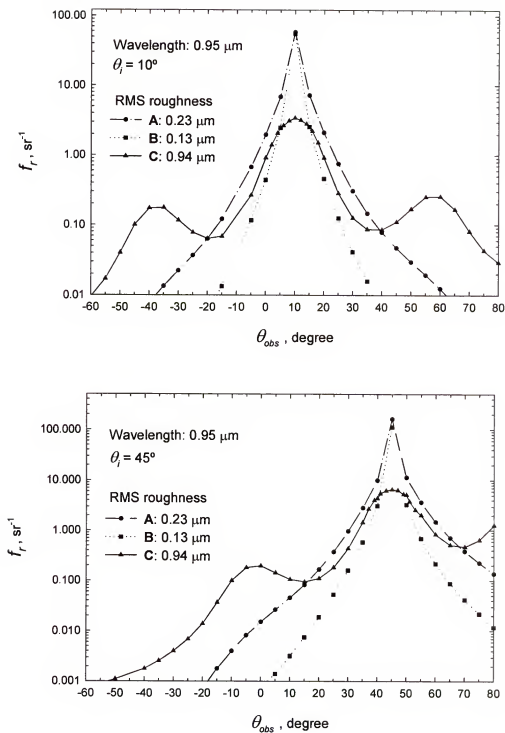


Figure 4-2 Comparison of the measured BRDF at $\lambda = 0.95 \mu\text{m}$ at incidence angle of 10° (upper) and 45° (lower).

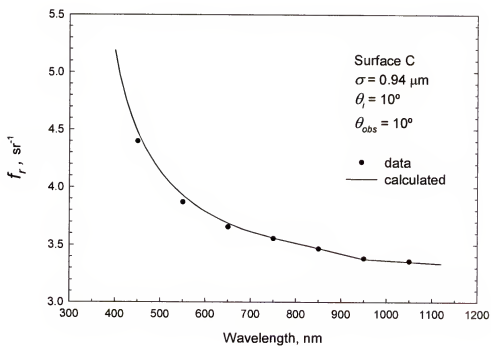
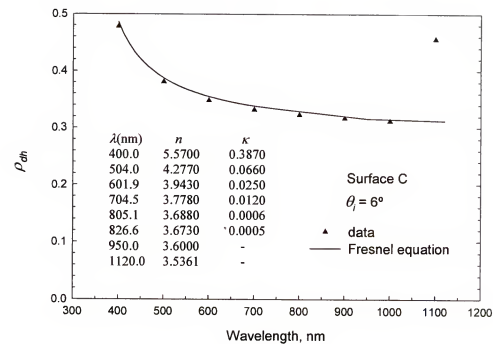


Figure 4-3 Directional-hemispherical reflectance (upper) and BRDF at the specular angle (lower) for surface C.

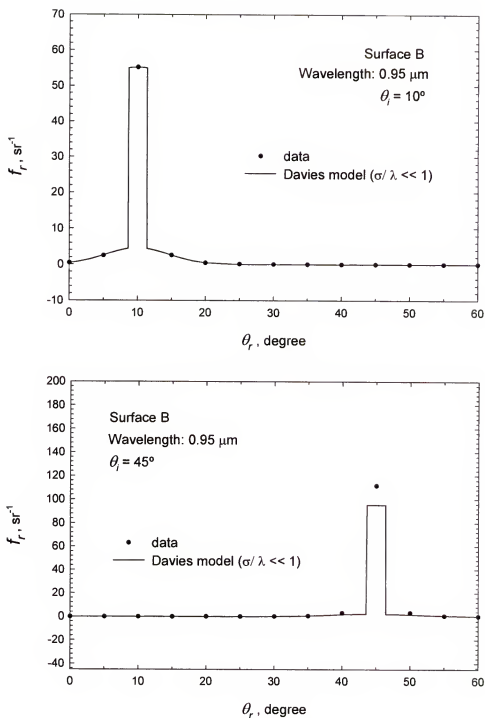


Figure 4-4 Comparison of the Davies model with experiments for surface B: fitted result for 10° incidence angle (upper), and calculated result for 45° incidence angle (lower).

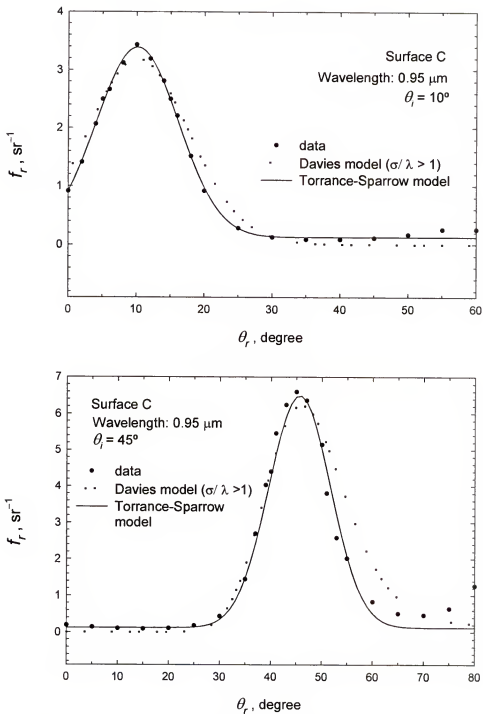


Figure 4-5 Comparison of the Davies model and Torrance-Sparrow model with experiments for surface C: fitted results for 10° incidence angle (upper), and calculated results for 45° incidence angle (lower).

CHAPTER 5 RESULTS FROM THE NEW SCATTEROMETER

5.1 Sample Characterization

A number of Si wafers with different surface roughness were used for the following study and discussion. Their configurations are as follows:

- #102: uncoated plain wafer, one-side polished, 200 mm diameter, 0.8 mm thickness
- #120: uncoated, double-side polished, 200 mm diameter, 0.8 mm thickness
- #201: uncoated, one-side polished, 100 mm diameter, 0.6 mm thickness

Surface roughness was characterized with the WYKO NT1000 optical interferometric profilometer. Several magnifications were tested and found that they have little effect on the roughness value (Zhu et al., 2002). The RMS roughness σ of the smooth side is 1 nm – 4 nm, which can be treated as optically smooth for the wavelengths used. The values of σ of the rough sides are 0.26 μm and 0.57 μm for samples #102 and #201, respectively. Their histogram plots (probability density vs. deviation from the mean level) are shown in Fig. 5-1. Sample #102 is shown as a Gaussian random rough surface. However, the profile of sample #201 deviates a little from the Gaussian rough surface. The effect of non-Gaussian surface to the scattering may need further investigation in the future. The autocorrelation length a can be estimated from the autocorrelation function, plotted in Fig. 5-2. The curve basically follows an exponential decay and the values of a are 3.20 μm and 4.18 μm for samples #102 and #201, respectively.

5.2 BRDF for Wavelengths of 635 nm and 785nm

The BRDF data versus reflection angles were recorded for different incidence

angles ($\theta_i = 15^\circ, 30^\circ, 45^\circ, 60^\circ$, and 75°). The results for sample #102 at $\lambda = 635$ nm are plotted in Fig. 5-3 for the incidence plane with $\phi_r - \phi_i = 180^\circ$. The presented data are unpolarized values averaged from the s and p polarization results. For an initial validation to the measurement, the reciprocity of BRDF can be observed. For example, the BRDF of 30° incidence and 45° reflection should be equal to that of 45° incidence and 30° reflection. We have not observed any off-specular peaks for this slightly rough surface. In addition, the log scale in the plot implies the surface is approaching to a mirror-like one when the incidence angle is large enough. Two out-of-plane data sets are also plotted in 3-D with the in-plane data (shown in Fig. 5-4). Generally, these BRDF data show that the backside of commercial silicon wafers can not be easily modeled as a combination of specular and perfectly diffuse components. The BRDF varies with incidence angles, reflection polar angles, and reflection azimuthal angles.

The comparisons of two wavelengths are shown in Figs. 5-5a and 5-5b for samples #102 and #201, respectively. For the slightly rough sample #102 ($\sigma/\lambda = 0.4$ for $\lambda = 635$ nm), the shorter wavelength gives a more attenuated specular peak and more off-specular scattering. Basically, this can be predicted by the reflectance models, which are discussed in the following sections. Conversely, the sample #201 ($\sigma/\lambda = 0.9$ for $\lambda = 635$ nm) shows a less dependence of these two employed wavelengths. The very sharp specular peaks disappear (Fig. 5-5b is with a linear coordinate). The scattering is distributed more to the directions out of the specular direction. A second peak with about 60% magnitude of the first peak is shown at about $\theta_r = 75^\circ$. The specular peak value for 785 nm is smaller than that for 635 nm due to diminished power reflection coefficient.

The ratio of the specular peak values for $\lambda = 635$ nm and 785 nm, 1.35, is within the same magnitude of order to the ratio of the hemispherical reflectances, 1.06.

5.3 Modeling Results

This section focuses on the results from a proposed empirical model and the comparisons to other theoretical models. By observing the measurement BRDF data, basically the curves can follow exponential decaying functions with different peak values and decaying rates. Therefore, an empirical equation is suggested as an exponential function with two parameters, shown as follows

$$f_r = \rho_{dh} a \exp\left[-\frac{|\theta_r - \theta_i|}{b}\right] \quad (5.1)$$

where ρ_{dh} is the directional hemispherical reflectance. The absolute difference of reflection angle and incidence angle means the angle deviation from the specular direction. The parameters a and b are obtained by the curve fitting to the measured data excluding the specular data point. The modeling results of sample #102 at 635 nm are shown in Fig. 5-6 for different incidence angles. The measured specular data points are not shown here and will be discussed separately. For sample #102, two sets of parameters a and b (Table 5-1) are used to match the BRDF distributions. One set, a_1 and b_1 , is for the reflection direction within approximate $5^\circ \sim 10^\circ$ from the specular direction. The other set, a_2 and b_2 , is for the directions outside that region. The results are good for most of incidence cases. The same approach is also applied to the 785 nm wavelength and sample #201. The fitting parameters of sample #102 are plotted in Fig. 5-7 for different incidence angles and wavelengths. The parameter a controls the peak value of the empirical equation. In Fig. 5-7a, the values of parameter a increase when the incidence

angle increases. The increase rate of 635 nm is a little larger than that of 785 nm. The parameter b represents the decaying rate of the empirical equation. A smaller b value tends to give a sharper BRDF distribution. In other words, a smaller b value gives a scattering distribution concentrated more near the specular direction. In Fig. 5-7b, the value of parameter b_1 decreases when the incidence angle increases and the value for 785 nm is smaller than that for 635 nm. However, the behavior of b_2 value for 785 nm implies for a larger incidence angle the scattering distribution decays more slowly far from the specular direction than that for 635 nm.

Different modeling results (shown in Fig. 5-8) are compared to the experimental BRDF data. The Davies model and the Torrence-Sparrow model are employed with some fitting parameters as the previous procedure. The ray-tracing results are from Zhou and Zhang (2002). Near the specular direction, the results of the empirical model, Davies model, and Torrence-Sparrow model match the measured data closely. The ray-tracing method is not very good for the near specular direction in this slightly rough surface case. For the reflection directions far from the specular direction, only the empirical model and ray-tracing method match the measured data. The advantage of this ray-tracing method is that a lot of simulation can be performed for different roughness conditions, which are controlled by only RMS roughness and autocorrelation length. The disadvantage is lack of a simple mathematical equation for quick calculations.

For the much rougher surface of sample #201, the results from different models are shown in Fig. 5-9. Besides the second peak, the empirical model basically follows the experimental data. As previously, the Torrence-Sparrow model is good for a very rough surface. In this case, this model only gives a constant diffuse component far from the

specular direction. In order to model the second peak, multiple scattering should be considered with a complicated shadowing function in the Torrance-Sparrow model.

To consider the specular peak of a slightly rough surface, the Beckmann-Spizzichino model, Eq. (2.22), and the Davies model, Eq. (2.23) are used to compare with the measured specular peak values. These two simple models can predict the specular reflectance by providing two surface parameters, RMS roughness σ and autocorrelation length a . Figure 5-10a shows the Beckmann-Spizzichino model result, which is obtained by tuning the σ value until the predicted specularity agrees with the measured specularity for large incidence angles. For large incidence angles, in this case for $\theta_i > 60^\circ$, the off-specular component in the model is negligible compared to the specular component. Therefore, in that region the model only depends on σ value. The fitting values of σ are $0.16 \mu\text{m}$, which is smaller than the value obtained from the optical profilometer (Wyko), $0.26 \mu\text{m}$. The other samples also have this kind of trend. The possible reason may be that the optical profilometer could resolve more profile features. The sample was also investigated by the stylus profilometer and the rms roughness obtained is $\sim 0.13 \mu\text{m}$, which is closer to the model fitting value. For small incidence angles, the off-specular component is dominant. This can be observed in Fig. 5-10b, which shows the specular component is not significant for small incidence angles. The value of parameter a , which only affects the off-specular component, is the value from the optical profilometer. From Fig. 5-10b, the off-specular result of Beckmann-Spizzichino model approximately matches the experimental data. However, the Davies model gives too strong off-specular scattering in this case. For different wavelengths, the Beckmann-Spizzichino model gives consistent results in this case for 635 nm and 785

nm. However, the validity to a broader spectrum needs more measurements under different wavelengths.

5.4 BRDF and BTDF for Wavelength of 1550 nm

At 1550 nm, the same samples employed previously are expected to behave smoother due to small σ/λ . Figure 5-11 shows the BRDF/BTDF of 30° incidence at the rough side for samples #102 and #201. Comparing these two samples, the rougher surface (#201) behaves with a more attenuated specular peak and more scattering at large off-specular directions. In Fig. 5-12, the BRDF results are compared to the 635 nm data. The off-specular values for 1550 nm are at the same level for 635 nm since at 1550 nm internal multiple reflection exists.

Under the same measurement condition except for the illuminated side, the results of reflection and transmission for normal incidence are shown in Fig. 5-13. When the smooth side is illuminated, the first surface reflection is concentrated at the specular direction. Part of the transmitted radiation is reflected by the second (rough) surface and transmitted through the first surface. This part is shown (Fig. 5-13a) very diffuse and smaller compared to the rough-side illuminated case. For $\theta_r > 50^\circ$, the reflection is a little stronger for the smooth-side illuminated case than that for the rough-side illuminated case. That may be due to any internal multiple reflection. The transmission distributions (Fig. 5-13b) do not show significant difference between the two cases. For the 30° incidence (shown in Fig. 5-14), the difference of reflection distributions for the two cases is similar to that for the normal incidence. The transmission distributions have barely measurable difference for off-direct directions between the two illumination cases.

In Fig. 5-15, the specular reflectance is plotted with different incidence angles. The measured data show that the scattering due to surface roughness is reduced for large incidence angles. The figure also includes theoretical calculations, using the thick-slab model (neglecting interference effects) with the roughness attenuation factors, described in Chapter 2. The prediction with $\sigma = 0.2 \mu\text{m}$ fits the measured data for sample #102 ($\sigma = 0.26 \mu\text{m}$) closely.

5.5 Out-of-plane Results

Typically, polar angle θ and azimuthal angle ϕ are used in the representation of BRDF and in the instrument control. However, it is easier to represent the out-of-plane BRDF by using the local coordinates according to a cone around the specular direction. The local polar angle θ' and the local azimuthal angle ϕ' have the following relations to the typical coordinates θ and ϕ :

$$\cos \theta_r = \cos \theta, \cos \theta' + \sin \theta, \sin \theta' \cos \phi' \quad (5.2a)$$

$$\sin \theta, \cos \phi_r = \cos \theta, \sin \theta' \cos \phi' - \sin \theta, \cos \theta' \quad (5.2b)$$

The local polar angle θ' can be treated as the off-specular angle with respect to the specular direction. The local azimuthal angle ϕ' tells the direction about the specular ray. The in-plane corresponds to $\phi' = 0^\circ$ and 180° . The condition of θ_r smaller than the specular angle is set for $\phi' = 0^\circ$.

The results of $\phi' = 0^\circ, 45^\circ, 90^\circ, 135^\circ$, and 180° for 30° incidence are plotted in Fig. 5-16a. The BRDF result for $\phi' = 180^\circ$ has the highest value. The figure shows the deviation of the curves is more significant for a larger off-specular angle ($\theta' > 5^\circ$). The result for the rougher sample (Fig. 5-16b) implies the deviation increases when θ'

increases. Nonetheless, it is appropriate to integrate the in-plane measurement results to obtain the ratio of power scattered within a small cone to the incident power. The BRDF is approximately isotropic about ϕ' directions within a small detection cone ($\theta' < 5^\circ$ in the above case).

The method of integrating the in-plane results to deduce the conical reflectance can be shown as follows if the BRDF is assumed isotropic about ϕ' (Drolen, 1992):

$$\rho(\theta_i, \omega_r) = 2\pi \cos \theta_i \int_0^{\theta_c} f_r \cos \theta' \sin \theta' d\theta' \quad (5.3)$$

where θ_c is the half-cone angle for a detection cone. Combining the empirical model of Eq. (5.1) with Eq. (5.3), a quick way to calculate the conical reflectance can be obtained in the following form:

$$\rho(\theta_i, \omega_r) = \frac{\pi a p_{dh} \cos \theta_i}{b^{-2} + 4} \left[2 - (b^{-1} \sin 2\theta' + 2 \cos 2\theta') \exp(-\theta' b^{-1}) \right] \quad (5.4)$$

Using the fitting parameter obtained previously, the results for 30° incidence at $\lambda = 635$ nm are calculated and plotted in Fig. 5-17 for the half-cone angle up to 5° . The conical reflectance is more sensitive to the half-cone angle for a smoother surface (with a sharper curve of BRDF). These results are also helpful to compare different BRDF instruments with different size of the detection cone.

Table 5-1 Parameters of the Empirical Model (Sample #102) for Different Incidence Angles and Wavelengths

Incidence angle, degree	15	30	45	60	75
a_1 for 635 nm, sr^{-1}	11.37	16.16	32.78	104.49	323.42
a_1 for 785 nm, sr^{-1}	14.93	21.85	43.77	112.46	230.92
a_2 for 635 nm, sr^{-1}	9.22	12.17	18.12	43.65	101.73
a_2 for 785 nm, sr^{-1}	9.84	12.92	14.66	32.20	49.31
b_1 for 635 nm, degree	7.68	6.79	5.09	3.30	2.53
b_1 for 785 nm, degree	5.74	5.04	3.84	2.94	2.44
b_2 for 635 nm, degree	9.16	8.65	8.47	6.95	5.49
b_2 for 785 nm, degree	8.33	8.11	9.41	7.92	5.98

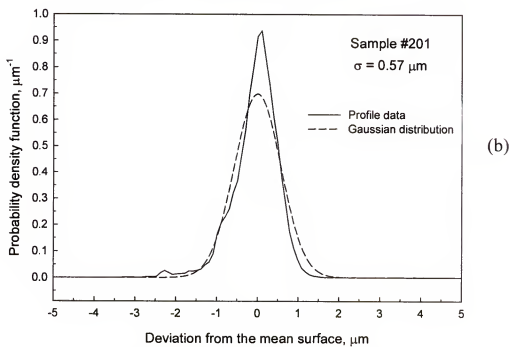
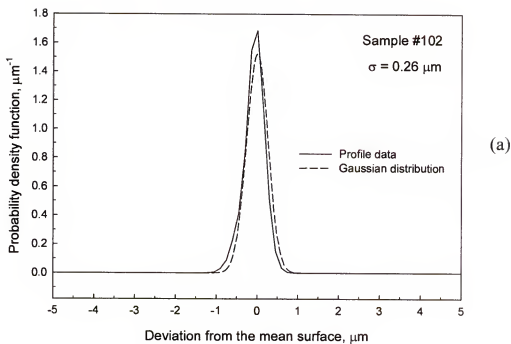


Figure 5-1 Histogram for samples (a) #102 and (b) #201.

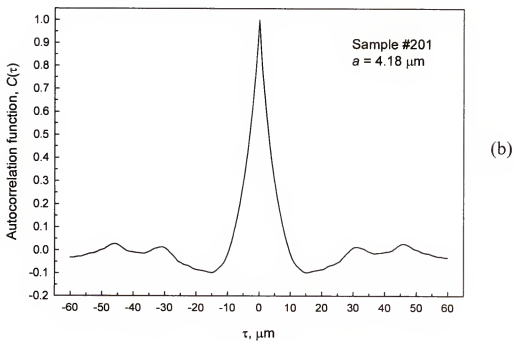
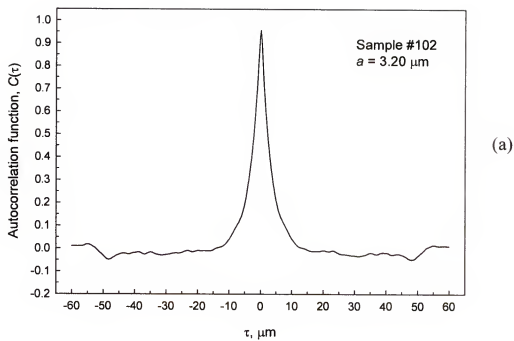


Figure 5-2 Plot of the autocorrelation function for samples (a) #102 and (b) #201.

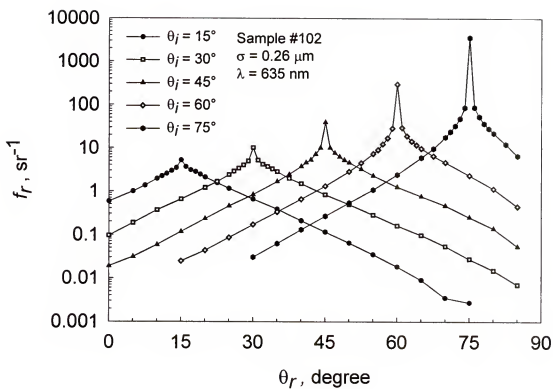


Figure 5-3 BRDF data for the rough surface #102 of $\varphi_r = 180^\circ$ with respect to $\varphi_i = 0^\circ$.

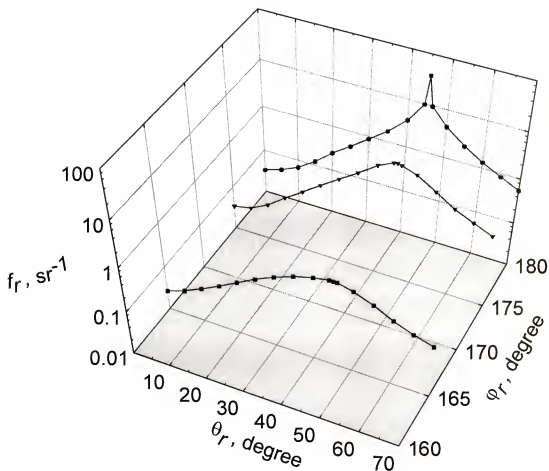


Figure 5-4 BRDF data of the rough surface #102 of $\phi_r = 165^\circ$, 175° , and 180° with respect to $\phi_i = 0^\circ$ and $\theta_i = 45^\circ$.

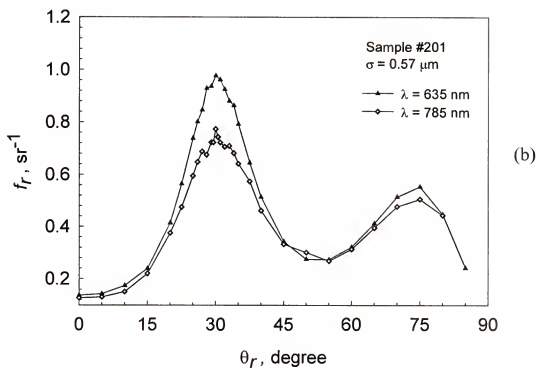
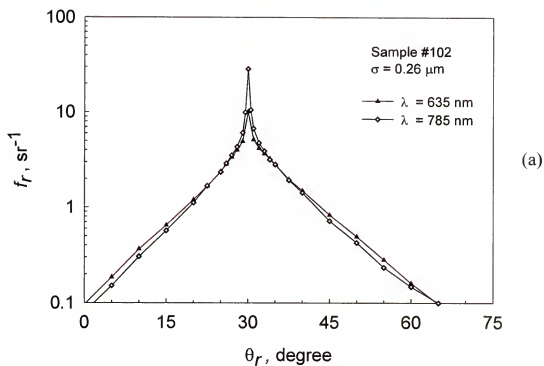


Figure 5-5 Comparison of BRDF data at different wavelengths for samples (a) #102 and (b) #201.

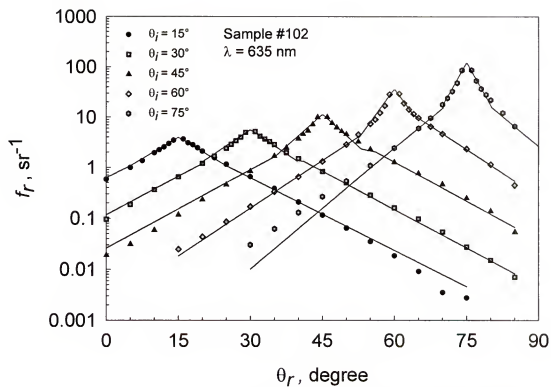


Figure 5-6 Empirical model result (solid line) with experimental data (dot) of sample #102.

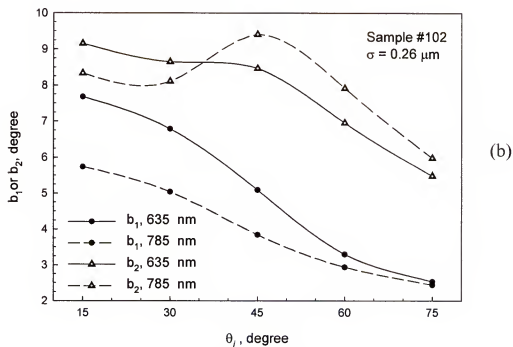
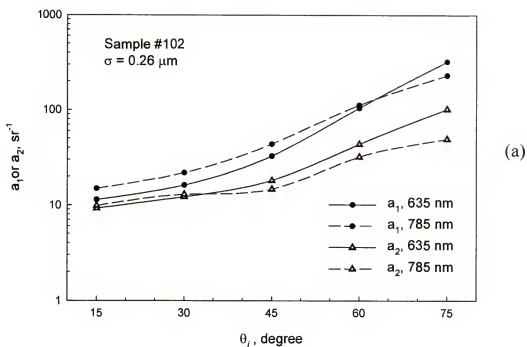


Figure 5-7 (a) parameters a and (b) parameter b of the empirical model for different incidence angles and wavelengths.

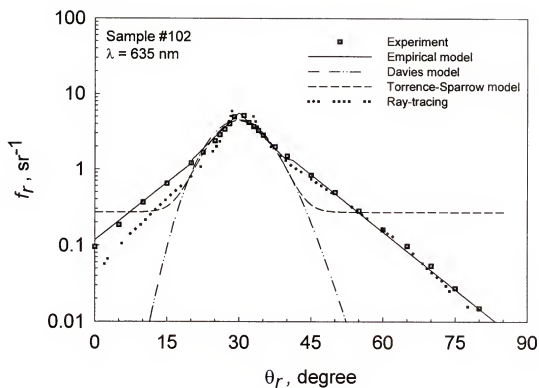


Figure 5-8 Comparison of different models and experimental data for sample #102.

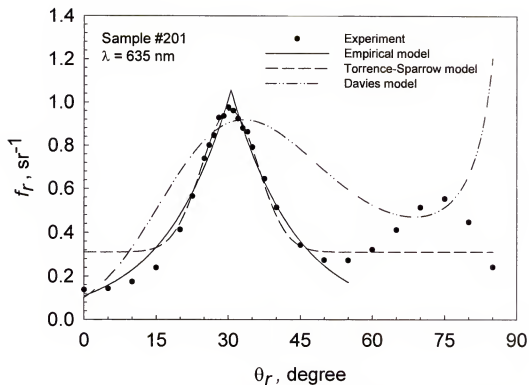


Figure 5-9 Comparison of different models and experimental data for sample #201.

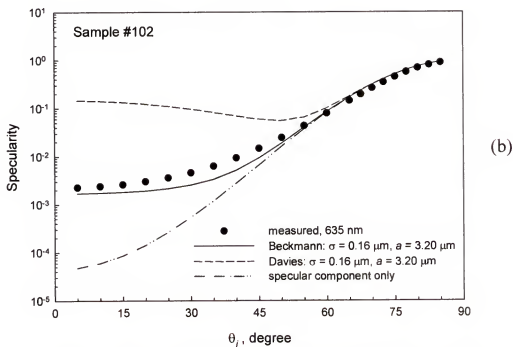
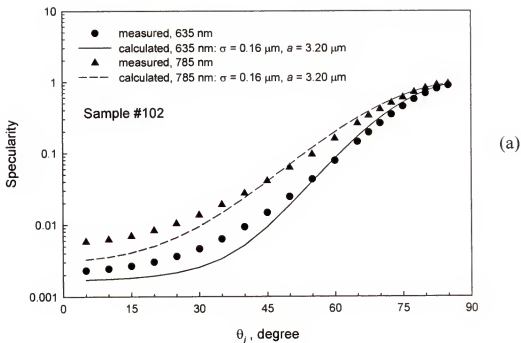


Figure 5-10 (a) Specularity data versus model results at two wavelengths; (b) Comparison of two models with experimental data.

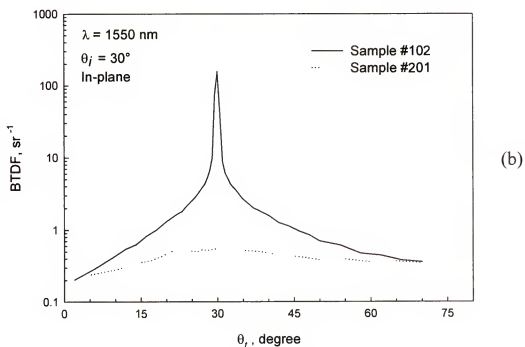
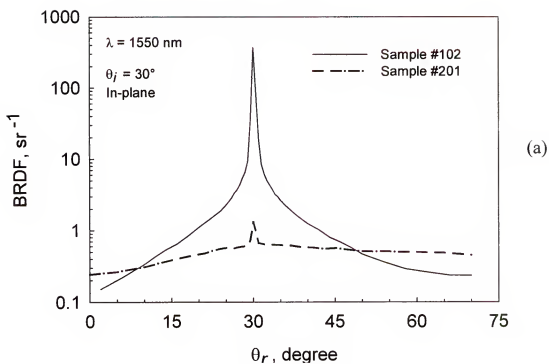


Figure 5-11 (a) BRDF data and (b) BTDF data at wavelength of 1550 nm.

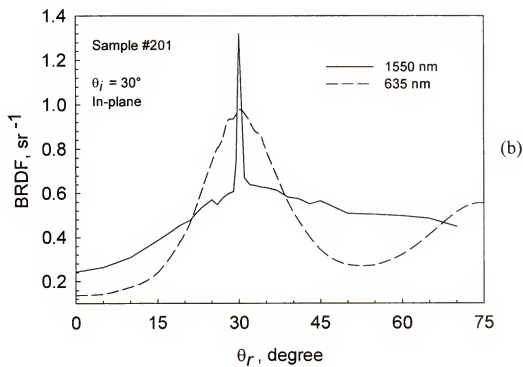
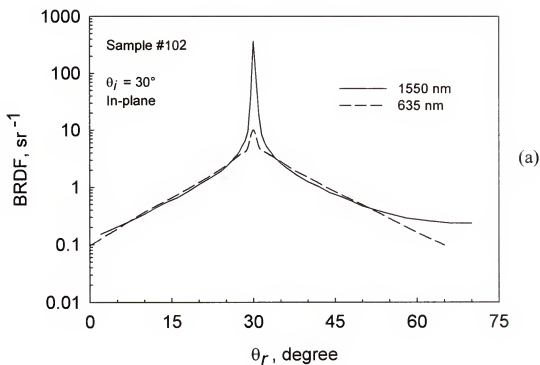


Figure 5-12 Comparison of BRDF at wavelengths of 635 nm and 1550 nm for samples (a) #102 and (b) #201.

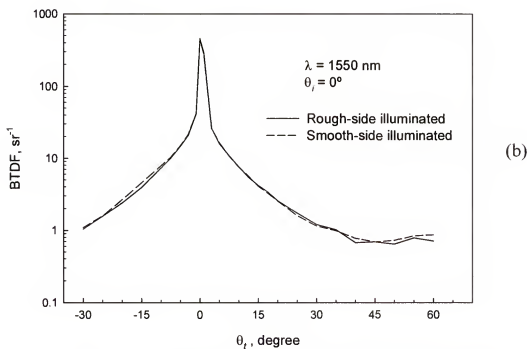
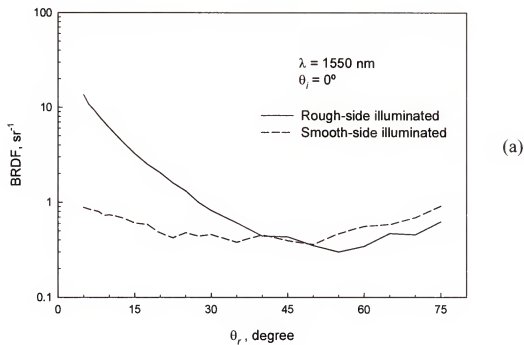


Figure 5-13 (a) BRDF and (b) BTDF data of illumination from different sides at 0° incidence.

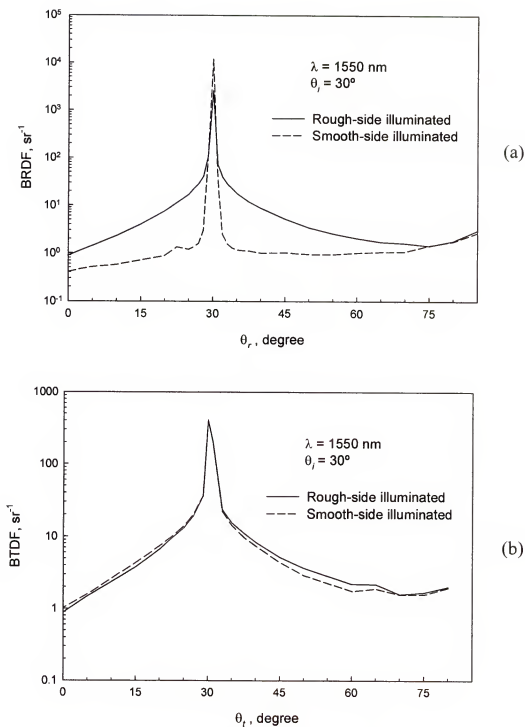


Figure 5-14 (a) BRDF and (b) BTDF data of illumination from different sides at 30° incidence.

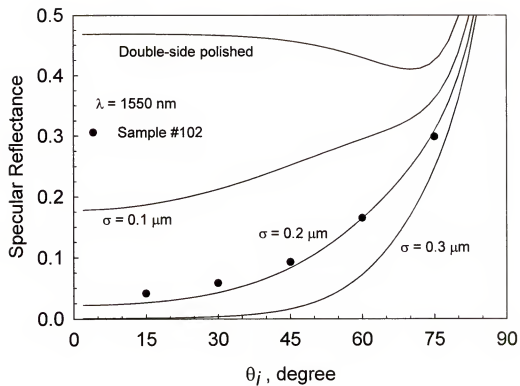


Figure 5-15 Specular reflectance of sample #102 with different incidence angles at wavelength of 1550 nm; theoretical calculations with different surface roughness are also shown.

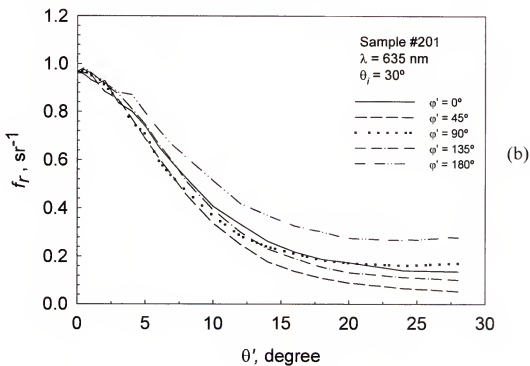
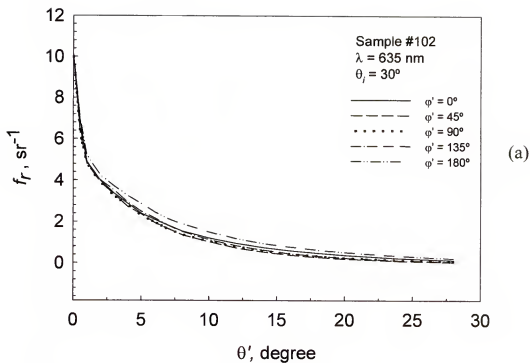


Figure 5-16 Out-of-plane results for samples (a) #102 and (b) #201.

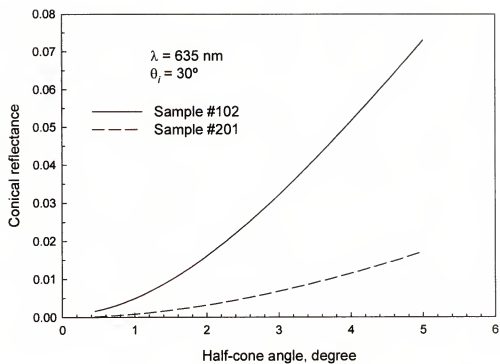


Figure 5-17 Calculation of conical reflectance for different half-cone angles.

CHAPTER 6 COMPARISONS OF THE NEW SCATTEROMETER WITH STARR AND *IN SITU* MEASUREMENTS

6.1 Comparison with Results from STARR

The reason to discuss the comparison with the STARR measurement after Chapter 5 is that the empirical model in section 5.3 and the method to evaluate conical reflectance in section 5.5 are applied to compare the specular peaks. The purpose of comparison is to evaluate the systematic uncertainty. Although the uncertainty has been evaluated in section 3.2 with ~2% uncertainty, the uncertainty due to misalignment and background stray light is difficult to evaluate. Therefore, the same samples used by the new scatterometer have been measured by STARR under the same wavelengths. Since this study focus on the unpolarization properties, only the average value of s and p polarization results are presented. The illumination position is kept as close as possible to the wafer center for both instruments.

At wavelength of 635 nm (Fig. 6-1), these two instruments basically give the same measurement results. Except for the specular peaks in the case of the slightly rough surface (sample #102), the differences are within about 5%. Hence, the uncertainty due to misalignment and stray noises is believed within the 5% level. That is a promising outcome for the new scatterometer because its detector field of view is much larger than the imaging system design of STARR and further design to reduce the field of view or to employ any beam blocks and special black paints has not yet been applied. For wavelength of 1550 nm (Fig. 6-2), both BRDF and BTDF values have more significant

differences (within about 10%) than for the 635 nm case. That implies that the stray light noise may be more significant at 1550 nm for the new scatterometer.

The specular peaks are typically not easy to be compared between different instruments. For a slightly rough surface, the peak value of BRDF may tend to depend on the size of collecting solid angle as in the case of mirror. Hence, the idea of conical reflectance around the specular direction is more suitable as the common ground of comparison. For sample #102, the result shows the new scatterometer gives higher peak values due to the smaller collecting solid angle. A quick comparison can be done by using the result in the previous subsection (Fig. 5-17). The half-cone angle of STARR is estimated as 1.35° . The corresponding conical reflectance is $8.15\text{E-}3$ based on the calculation of Eq. (5.4) for the case of 30° incidence. Checking the measured value ($8.13\text{E-}3$) by STARR, the relative difference is only 0.25%. The relative difference of reflectance measurements at the specular direction is small with respect to the off-specular measurements for the case of slightly rough surface.

6.2 Comparison with Results from the *In Situ* Measurement

In the *in situ* experiment, the specular directional-conical reflectance and regular directional-conical transmittance were measured. Using these measured BRDF and BTDF, *ex situ* conical properties for the purpose of comparison are obtained by Eqs. (2.16a) and (2.16b) with the corresponding solid angles of the *in situ* setup.

The *in situ* reflectance $\rho(\theta_i; \omega_r)$ results using the 635 nm diode laser are shown in Table 6-1. The incidence angle is 30° and the reflection measurement is at the specular direction within the incidence plane. Measurements were made using both s and p polarized light and the average reflectances are shown in the table. For sample #120 and

for the smooth side of samples #102, the measured reflectance is between 0.34 and 0.35. The difference between the *in situ* and *ex situ* measurements is ~1-2%.

For the rough surface, the reflectance is significantly reduced with respect to the smooth surface results as a result of surface roughness. An apparent difference is observed between *in situ* and *ex situ* values for the rough surface of #102. This could be caused by the limited accuracy of the integration that results from an insufficient number of *ex situ* BRDF data points near the specular peak.

It is noteworthy that because the aluminum top and bottom plates are far away from the wafer, the effect of reflection by the aluminum plates on the specular reflectance should be negligible. For rough surfaces at off-specular reflection angles, the reflected signal is small and the chamber effects may become important.

The measurement on double-side polished sample #120 was used to verify the measurement accuracy by making a comparison to the result from a theoretical calculation of the thick-slab model (neglecting interference effects) as the following equations

$$R = \rho \left[1 + \frac{(1-\rho)^2 \tau^2}{1-\rho^2 \tau^2} \right] \quad (6.1a)$$

and

$$T = \frac{(1-\rho)^2 \tau}{1-\rho^2 \tau^2} \quad (6.1b)$$

For silicon the refractive index is 3.48 and extinction coefficient is ~ 0 at 1550 nm (Edwards, 1985), so the surface reflectance, $\rho = 0.306$ and the internal transmittance, $\tau \approx 1$, for normal incidence. The reflectance, R, and transmittance, T, of the wafer are

calculated as 0.469 and 0.531, respectively. The calculated transmittance agrees well with the measured value of 0.532 for sample #120. This shows that the measurement at 1550 nm is reliable even though the optical alignment is difficult in the infrared range.

For the one-side polished wafers it was found that there is not much difference in the measured transmittances regardless of whether the wafers are illuminated from the smooth side or rough side. Comparison of the results for #102 and #120 shows that the scattering effect due to the rough surface causes the measured transmission of the one-side polished wafer to reduce by nearly an order of magnitude relative to that for double-side polished wafers.

More results, including reflectance and transmittance, are shown in Table 6-2 for 30° incidence with $\theta_r = \theta_t = 30^\circ$ in the plane of incidence. Again, we can observe that for the one-side polished wafers there is not much difference in the measured transmittances regardless of whether they are illuminated from the smooth side or rough side. However, the reflectance results show large differences between these cases. The measured (specular) reflectance is greatly reduced when the light is incident on the rough side. As before, the measured transmittance is reduced for one-side polished wafers. As was the case in the results of 635 nm, an apparent difference is observed between *in situ* and *ex situ* measurements of the rough surfaces.

Table 6-1 Specular reflectance measured with the 635 nm diode laser source at an incidence angle of $\theta_i = 30^\circ$.

Sample I.D.	#102 smooth side	#102 rough side	#120 (both side smooth)
Reflectance <i>In situ</i>	0.343	0.014	0.349
Reflectance <i>Ex situ</i>	0.341	0.016	0.343

Table 6-2 Results for the 1550 nm light source, $\theta_i = 30^\circ$ and $\theta_r = \theta_t = 30^\circ$ in the plane of incidence.

Sample I.D.	#102 smooth side illuminated	#102 rough side illuminated	#120	Calculation for double-side polished
Reflectance <i>In situ</i>	0.300	0.081	0.457	0.467
Reflectance <i>Ex situ</i>	0.303	0.078	-	
Transmittance <i>In situ</i>	0.041	0.042	0.530	0.533
Transmittance <i>Ex situ</i>	-	0.052	-	

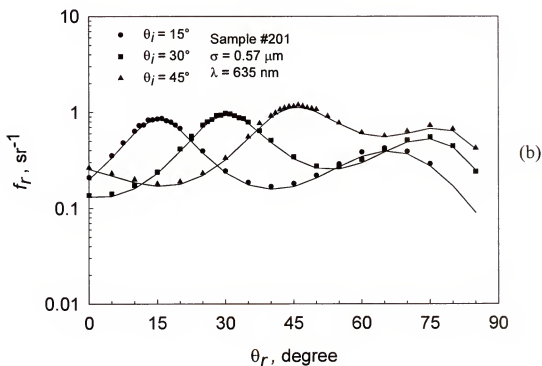
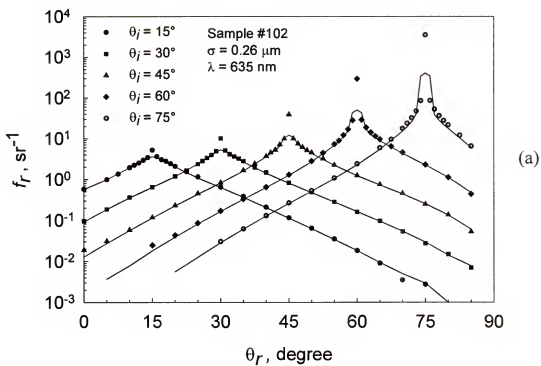


Figure 6-1 Comparison to the STARR results (solid line) for (a) samples #102 and (b) #201 at wavelength of 635 nm.

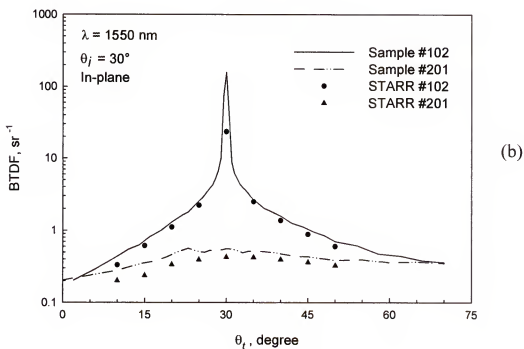
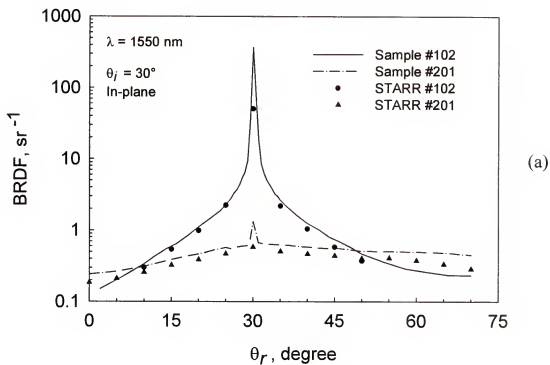


Figure 6-2 Comparison to the STARR results for (a) BRDF and (b) BTDF at wavelength of 1550 nm.

CHAPTER 7

CONCLUSIONS AND RECOMMENDATIONS

Initially, the BRDFs of several silicon wafers with different surface roughness were measured by STARR at NIST. Two simplified models, categorized as the Kirchhoff approximation and the geometrical-optics approximation, were applied to fit the BRDF data. Reasonable agreement exists between the measured data and the model results without considering the coating effect. For an initial study of rapid thermal processing systems, these simple formulae could be incorporated into the Monte Carlo model to evaluate the effect of rough surfaces.

A new bidirectional scatterometer has been built and tested. The features include stability of the light source, incident light monitoring, modulated light output by the diode laser current controller, and capability of out-of-plane and BTDF measurements. By the comparison to the results from STARR of NIST, the relative difference is within the level of 5% for wavelengths of 635 and 785 nm and of 10% for 1550 nm.

The specularities of different rough surfaces can be matched approximately by the Beckmann-Spizzichino model. For the semi-transparent case at 1550 nm, the specular reflectance can be also estimated by the modified thick-slab model with roughness attenuation factors. A simple form of exponential function with two parameters was proposed as an empirical model to fit the measured BRDF data. Sets of the parameters were obtained for two studied samples at wavelengths of 635 and 785 nm. This approach represents the measured data better than some other existing theoretical models discussed

in this thesis. The empirical approach is justified and proper to serve as a tool to analyze and represent experimental data for a certain range of rough wafers.

By combining the empirical model and the integration of BRDF with the angle transformation, an analytical form of conical reflectance can be employed as a quick way to compare the specular peak measurements of different instruments with varied collecting half-cone angles.

Although the alignment is tedious for the *in situ* setup, reasonable measurement results of the wafer transmittance and reflectance in the mock-up chamber are obtained. The effect due to the chamber is not apparent in the past measurements. It may become important for nonspecular reflection directions, at which the signal is small.

Some recommendations for instrumentation design and measurement based on the experience of this study are summarized as follows. A more accurate alignment method is helpful for the infrared source. The effect of an enlarged illumination area due to a large incidence angle may need some quantitative investigation if the sample is not uniform with respect to the illumination size. One should care more about the breakdown of diode laser due to overdriven current or thermal issues. An additional compact automatic rotary stage for the polarizer can save measurement time. An imaging detector system with a confined field of view may be helpful to minimize stray light noise. One should be careful about any sample distortion caused by sample holder clamping. A curved surface may affect measurement results severely. The out-of-plane and large incidence angle measurements are often overlooked. The former is important to verify the data symmetry for different surface conditions. The latter may have an impact to the future *in situ* metrology for RTP systems. Because a probe or source may be inserted from the side

wall of a processing chamber, the chamber geometry hardly prevents the situation with large incidence and viewing angles. Characterization of a surface profile is recommended to be obtained by repeating several times and employing some different profilometers to minimize the measurement errors.

APPENDIX ANGLE TRANSFORMATION

For a general gimbal system, shown in Fig. A-1, a sample is rotated, tilted, and orientated with respect to three axes by the angles of a , b , c . A fixed-frame coordinate at the sample origin is defined as $\{\hat{x}', \hat{y}', \hat{z}'\}$. As defined in the BRDF geometry, the polar (θ) and azimuthal (ϕ) angles are according to the sample coordinate $\{\hat{x}, \hat{y}, \hat{z}\}$, shown in Fig. A-2. The sample coordinate system is initially set to be coincident with the fixed-frame coordinate when $a = b = c = 0$. The transformation of these two coordinate systems is based on the fundamental rule of rotation with respect to axis \hat{z} , shown in Fig. A-3:

$$x' = x \cos \theta + y \sin \theta \quad (\text{A.1a})$$

$$y' = y \cos \theta - x \sin \theta \quad (\text{A.1b})$$

$$z' = z \quad (\text{A.1c})$$

The procedure of transformation for the gimbal system has three steps: (1) rotating $\{\hat{x}', \hat{y}', \hat{z}'\}$ about \hat{y}' with a ; (2) rotating the new coordinate about the new x axis with b ; (3) rotating the new coordinate about the new z axis with c . Then, the (x, y, z) can be represented by (x', y', z') and (a, b, c) as

$$\begin{aligned} x = & (\cos a \cos c + \sin a \sin b \sin c)x' + (\cos b \sin c)y' \\ & + (\cos a \sin b \sin c - \sin a \cos c)z' \end{aligned} \quad (\text{A.2a})$$

$$\begin{aligned} x = & (\sin a \sin b \cos c - \cos b \sin c)x' + (\cos b \sin c)y' \\ & + (\sin a \sin c + \cos a \sin b \cos c)z' \end{aligned} \quad (\text{A.2b})$$

$$x = (\sin a \cos b)x' - (\sin b)y' + (\cos a \cos b)z' \quad (\text{A.2c})$$

For the goniometric system employed in this study (Chapter 3), shown in Fig. A-4, the simplification is $b = c = 0$ in the above equations. The reflection direction (detector position) can be represented in $\{\hat{x}', \hat{y}', \hat{z}'\}$ as $(\cos\beta\sin\gamma, \sin\beta, \cos\beta\cos\gamma)$. By the above transformation using $a = \alpha$, it is equal to $(\cos\beta\sin(\gamma-\alpha), \sin\beta, \cos\beta\cos(\gamma-\alpha))$ in $\{\hat{x}, \hat{y}, \hat{z}\}$. Again by the definition in Fig. A-2, the reflection direction is also $(\sin\theta_r \cos\varphi_r, \sin\theta_r \sin\varphi_r, \cos\theta_r)$ in $\{\hat{x}, \hat{y}, \hat{z}\}$. Then, the relationship between (θ_r, φ_r) and (α, β, γ) can be derived as

$$\cos\theta_r = \cos(\gamma - \alpha)\cos\beta \quad (\text{A.3a})$$

$$\cos\varphi_r \sin\theta_r = \sin(\gamma - \alpha)\cos\beta \quad (\text{A.3b})$$

$$\sin\varphi_r \sin\theta_r = \sin\beta \quad (\text{A.3c})$$

If φ_r is constrained between 0 to π , Eq. (A.3b) is sufficient to fully determine it by given (α, β, γ) .

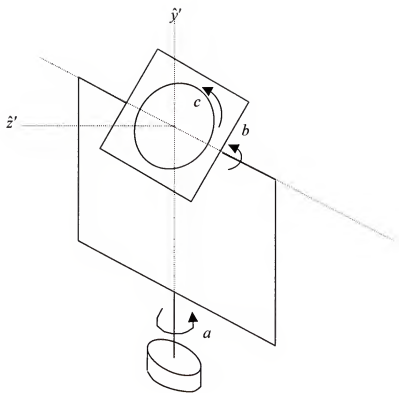


Figure A-1 Coordinates of a gimbal system.

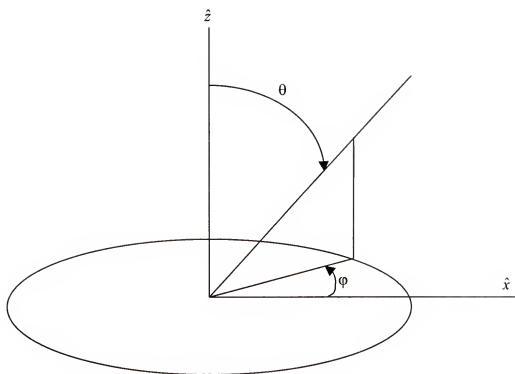


Figure A-2 Coordinates of a sample.

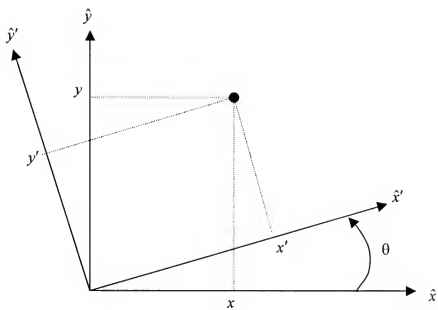


Figure A-3 Coordinate transformation.

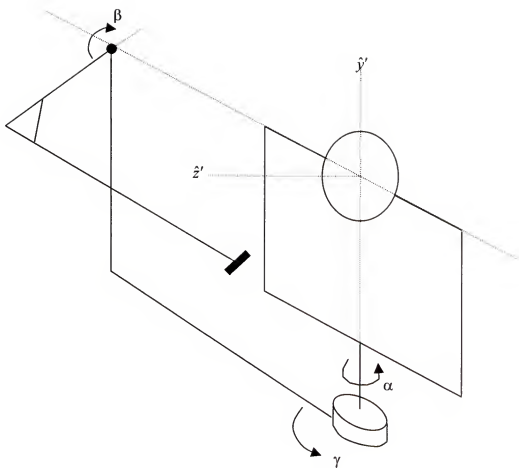


Figure A-4 Coordinates of the new goniometric system in Chapter 3.

REFERENCES

- American Society for Testing and Materials (ASTM), 1997, *Standard Practice for Angle Resolved Optical Scatter Measurements on Specular or Diffuse Surfaces*, Publication E1392-96.
- S. Anderson, S.M. Pompea, D.F. Shepard, and R. Castonguay, 1988, "Performance of a Fully Automated Scatterometer for BRDF and BTDF Measurements at Visible and Infrared Wavelengths," *Proc. SPIE*, vol. 967, pp. 159-170.
- P.Y. Barnes, E.A. Early, and A.C. Parr, 1998, *Spectral Reflectance*, NIST Special Publication 250-48, US Government Printing Office, Washington, DC.
- P. Beckmann and A. Spizzichino, 1963, *The Scattering of Electromagnetic Waves from Rough Surfaces*, Macmillan, New York.
- H.E. Bennett and J.O. Proteus, 1961, "Relation Between Surface Roughness and Specular reflectance at Normal Incidence," *Journal of the Optical Society of America*, vol. 51, pp. 123-129.
- B. Bhushan, 2001, "Surface Roughness Analysis and Measurement Techniques," *Modern Tribology Handbook*, B. Bhushan, ed., CRC Press, Boca Raton, FL, chap. 2.
- M. Bjuggren, L. Krummenacher, and L. Mattsson, 1997, Characterization of Engineering Surfaces by Infrared Scattering, *Optical Engineering*, vol. 36, pp. 874-882.
- J.G. Burnell, J.V. Nicholas, and D.R. White, 1995, "Scattering Model for Rough Oxidized metal Surfaces Applicable to radiation Thermometry of Reformer Furnaces," *Optical Engineering*, vol. 34, pp. 1749-1755.
- P.J. Caber, 1993, "Interferometric Profiler for Rough Surfaces," *Applied Optics*, vol. 32, pp. 3438-3441.
- E.I. Chaikina, R. Hernández-Walls, and E.R. Méndez, 1997, "Scattering by Randomly Rough Two-Dimensional Dielectric Surfaces," *Proc. SPIE* vol. 3141, pp. 164-169.
- E.L. Church and P.Z. Takacs, 1995, "Surface Scattering," *Handbook of Optics, Volume 1*, 2nd Ed., M. Bass, editor in chief, McGraw-Hill, New York, chap. 7.
- H. Davies, 1954, "The Reflection of Electromagnetic Waves from a Rough Surface," *Proc. IEE.*, vol. 101, pp. 209-214.

D.P. DeWitt, F.Y. Sorrell, and J.K. Elliott, 1997, "Temperature Measurement Issues in Rapid Thermal Processing," *Materials Research Society Symposium Proceedings*, vol. 470, pp. 3-15.

B.L. Drolen, 1992, "Bidirectional Reflectance and Specularity of Twelve Spacecraft Thermal Control Materials," *Journal of Thermophysics and Heat Transfer*, vol. 6, pp. 672-679.

D.F. Edwards, 1985, "Silicon (Si)," *Handbook of Optical Constants of Solids*, E.D. Palik, ed., Academic Press, Orlando, Florida, pp. 547-569.

X. Feng, J.R. Schott, and T. Gallagher, 1993, "Comparison of Methods for Generation of Absolute Reflectance-Factor Values for Bidirectional Reflectance-Distribution Function Studies," *Applied Optics*, Vol. 32, pp. 1234-1242.

I. Filinski, 1972, "The Effects of Sample Imperfections on Optical Spectra," *Physica Status Solidi B*, Vol. 49, pp. 577-588.

J.L. Garcia, 2002, *Design of a Heated Sample Holder and Measurements of Radiative Properties of Rough Silicon at High Temperatures*, Master Thesis, University of Florida, Gainesville, FL.

T.A. Germer and C.C. Asmail, 1999, "Goniometric Optical Scatter Instrument for Out-of-Plane Ellipsometry Measurements," *Review of Scientific Instruments*, vol. 70, pp. 3688-3695.

D.P. Greenberg, K.E. Torrance, P. Shirley, J. Arvo, J.A. Ferwerda, S. Pattanaik, E. Lafortune, B. Walter, S.-C. Foo, and B. Trumbore, 1997, "A Framework for Realistic Image Synthesis," *SIGGRAPH 97*, Association for Computing Machinery, Annual Conference Series, pp. 477-494.

B. Hapke, 1993, *Theory of Reflectance and Emittance Spectroscopy*, Cambridge University Press, Cambridge, UK, chap. 12.

R.G. Hering and T.F. Smith, 1970, "Surface Roughness Effects on Radiant Transfer between Surfaces," *International Journal of Heat and Mass Transfer*, vol. 13, pp. 725-739.

A.F. Houchens and R.G. Hering, 1967, "Bidirectional Reflectance of Rough Metal Surfaces," *Progress in Astronautics and Aeronautics*, vol. 20, pp. 65-89.

J.Q. Lu and A.A. Maradudin, 1997, "Surface Plasmon Polaritons in Light Scattering from Free-Standing Random Rough Thin Metal Films," *Proc. SPIE* vol. 3141, pp. 186-194.

S.H.C.P. McCall, 1998, "Bidirectional Reflectance Distribution Function as a Measure of Optical Scatter," *Applied Spectroscopy*, J. Workman, Jr. and A.W. Springsteen, eds., Academic Press, Chestnut Hill, MA, chap. 10.

S.H.C.P. McCall, 2001, "The Importance of Scatter in Stray Light Analysis," *Optics and Photonics News*, November, pp. 40-47.

M.F. Modest, 1993, *Radiative Heat Transfer*, McGraw-Hill, New York, chap. 2.

J.F. Murray-Colemann and A.M. Smith, 1990, "The Automated Measurement of BRDFs and Their Application to Luminaire Modeling," *J. Illum. Eng. Soc.*, vol. 19, pp. 87-99.

F.E. Nicodemus, 1970, "Reflectance Nomenclature and Directional Reflectance and Emissivity," *Applied Optics*, vol. 9, pp. 1474-1475.

A.G. Olszak, J. Schmit, and M.G. Heaton, 2001, "Interferometric Approaches Each Have Advantages," *Laser Focus World*, September, pp. 93-95.

W.H. Press, S.A. Teukolsky, W.T. Vetterling, and B.P. Flannery, 1992, *Numerical Recipes*, 2nd Ed., Cambridge University Press, New York, chap. 15.

J.E. Proctor and P.Y. Barnes, 1996, "NIST High Accuracy Reference Reflectometer-Spectrophotometer," *J. Res. Natl. Inst. Stand. Technol.*, vol. 101, pp. 619-627.

F. Rosa, Y.H. Zhou, Z.M. Zhang, D.P. DeWitt, and B.K. Tsai, 1999, "Modeling Chamber Radiation Effects on Radiometric Temperature Measurement in rapid thermal Processing," *Advanced in Rapid Thermal Processing*, F. Roozeboom, J.C. Gelpey, M.C. Öztürk, and J. Nakos, eds., The Electrochemical Society, Pennington, New Jersey, Proc. Vol. 99-10, pp. 419-426.

S. Roy, S.Y. Bang, M.F. Modest, and V.S. Stubican, 1993, "Measurement of Spectral, Directional Reflectivities of Solids at High Temperatures Between 9 and 11 μm ," *Applied Optics*, vol. 32, pp. 3550-3558.

Y.J. Shen, Z.M. Zhang, B.K. Tsai, and D.P. DeWitt, 2001, "Bidirectional Reflectance Distribution Function of Rough Silicon Wafers," *International Journal of Thermophysics*, vol. 22, pp. 1311-1326.

Y.J. Shen and Z.M. Zhang, 2002, "Design and Characterization of a Bidirectional Reflectometer," to be presented at the 12th International Heat Transfer Conference, Grenoble, France.

Y.J. Shen, Q.Z. Zhu, Z.M. Zhang, and P.J. Timans, 2002, "Reflectance and Transmittance Measurements in a Mock-Up Rapid thermal Processing Chamber," the 201st Meeting of the Electrochemical Society, May 12-17, Philadelphia, PA.

R. Siegel and J.R. Howell, 1992, *Thermal Radiation Heat Transfer*, 3rd Ed., Taylor & Francis, Washington, DC, chap. 3.

B.J. Stagg and T.T. Charalampopoulos, 1991, "Surface-roughness Effects on the Determination of Optical Properties of Materials by the Reflection Method," *Applied Optics*, vol. 30, pp. 4113-4118.

J.C. Stover, 1995, *Optical Scattering*, SPIE Optical Engineering Press, Bellingham, WA, chap. 6.

J.C. Stover, M.L. Bernt, E.L. Church, and P.Z. Takacs, 1994, "Measurement and Analysis of Scatter from Silicon Wafers," *Proc. SPIE*, vol. 2260, pp. 182-191.

K.Tang, Y. Yang, and R.O. Buckius, 1999, "Theory and Experiments on Scattering from Rough Interfaces," *Annual Review of Heat Transfer*, C.L. Tien, ed., Begell House, New York, vol. 10, chap. 3.

T.R. Thomas, 1999, *Rough Surfaces*, 2nd Ed., Imperial College Press, London, UK.

P.J. Timans, 1996, *Advances in Rapid Thermal and Integrated Processing*, F. Roozeboom, ed., Kluwer Academic Publishers, Dordrecht, The Netherlands, chap. 2.

P.J. Timans, R. Sharangpani, and R.P.S. Thakur, 2000, "Rapid Thermal Processing," *Handbook of Semiconductor Manufacturing Technology*, Y. Nishi, ed., Marcel Dekker, New York, pp. 201-286.

K.E. Torrance and E.M. Sparrow, 1967, "theory for Off-Specular Reflection from Roughened Surfaces," *Journal of the Optical Society of America*, vol. 57, pp. 1105-1114.

D.R. White, P. Saunders, S.J. Bonsey, J. van de Ven, and H. Edgar, 1998, "Reflectometer for measuring the Bidirectional Reflectance of Rough Surfaces," *Applied Optics*, vol. 37, pp. 3450-3454.

P.V. Zant, 2000, *Microchip Fabrication*, 4th Ed., McGraw-Hill, New York, chap. 3.

J.R. Zaworski, J.R. Welty, and M.K. Drost, 1996a, "Measurement and Use of Bi-directional Reflectance," *International Journal of Heat and Mass Transfer*, vol. 39, pp. 1149-1156.

J.R. Zaworski, J.R. Welty, B.J. Palmer, and M.K. Drost, 1996b, "Comparison of Experiment with Monte Carlo Simulations on a Reflective Gap Using a Detailed Surface Properties Model," *Journal of Heat Transfer*, vol. 118, pp. 388-393.

Z.M. Zhang, 2000, "Surface Temperature Measurement Using optical Techniques," *Annual Review of Heat Transfer*, C.L. Tien, ed., Begell House, New York, vol. 11, chap. 6.

Y.H. Zhou, Y.J. Shen, Z.M. Zhang, B.K. Tsai, and D.P. DeWitt, 2002, "A Monte Carlo Model for Predicting the Effective Emissivity of the Silicon Wafer in Rapid Thermal

Processing Furnaces,” *International Journal of Heat and Mass Transfer*, vol. 45, pp. 1945-1949.

Y.H. Zhou, Z.M. Zhang, D.P. DeWitt, and B.K. Tsai, 2001, “Effects of Radiative Properties of Surfaces on Radiometric Temperature Measurement,” Proceedings of the 9th International Conference on Advances Thermal Processing of Semiconductors - RTP 2001, pp. 179-188, September 25-29, Anchorage, Alaska.

Y.H. Zhou and Z.M. Zhang, 2002, “Radiative Properties of Semitransparent Silicon Wafers with Rough Surfaces,” Submitted to *Journal of Heat Transfer*.

Q.Z. Zhu, S. Sin, and Z.M. Zhang, 2002, “Surface Characterization of the Rough Side of Silicon Wafers,” to be presented in the 21st Southeastern Conference on Theoretical and Applied Mechanics, Orlando, Florida, May 19-21.

R.B. Zipin, 1966, “A Preliminary Investigation of the Bidirectional Spectral Reflectance of V-Grooved Surfaces,” *Applied Optics*, vol. 5, pp. 1954-1957.

BIOGRAPHICAL SKETCH

Yu-Jiun Shen was born in Taipei, Taiwan, disputedly named the Republic of China. He received his Bachelor of Science degree in Mechanical Engineering from the National Chung-Hsing University in June 1994. He served in the Army Aviation of Taiwan from August 1994 to June 1996. He was a corporal in charge of helicopter maintenance and assistance to a staff officer.

In Fall 1997 he came to Gainesville with his wife for their graduate studies at the University of Florida. Instructed by his advisor, Dr. Zhuomin Zhang, in the summer of 1998, Yu-Jiun performed thermal modeling of solar radiometers for a future satellite mission through a grant from the National Institute of Standards and Technology. In Summer 1999 he started the not-so-long pursuit of his Ph.D. degree. He worked on Dr. Zhang's career award project supported by NSF (CTS-9875441).

Yu-Jiun is a member of ASME, SPIE, and the Gainesville Chinese Christian Church.

I certify that I have read this study and that in my opinion it conforms to acceptable standards of scholarly presentation and is fully adequate, in scope and quality, as a dissertation for the degree of Doctor of Philosophy.



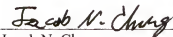
Zhuomin Zhang, Chairman
Associate Professor of Mechanical
Engineering

I certify that I have read this study and that in my opinion it conforms to acceptable standards of scholarly presentation and is fully adequate, in scope and quality, as a dissertation for the degree of Doctor of Philosophy.



D. Yogi Goswami
Professor of Mechanical Engineering

I certify that I have read this study and that in my opinion it conforms to acceptable standards of scholarly presentation and is fully adequate, in scope and quality, as a dissertation for the degree of Doctor of Philosophy.



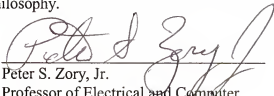
Jacob N. Chung
Eminent Scholar of Mechanical
Engineering

I certify that I have read this study and that in my opinion it conforms to acceptable standards of scholarly presentation and is fully adequate, in scope and quality, as a dissertation for the degree of Doctor of Philosophy.



David W. Hahn
Assistant Professor of Mechanical
Engineering

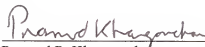
I certify that I have read this study and that in my opinion it conforms to acceptable standards of scholarly presentation and is fully adequate, in scope and quality, as a dissertation for the degree of Doctor of Philosophy.



Peter S. Zory, Jr.
Professor of Electrical and Computer
Engineering

This dissertation was submitted to the Graduate Faculty of the College of Engineering and to the Graduate School and was accepted as partial fulfillment of the requirements for the degree of Doctor of Philosophy.

December 2002



Pramod P. Khargonekar
Dean, College of Engineering

Winfred M. Phillips
Dean, Graduate School